Front. Struct. Civ. Eng. 2025, 19(8): 1240–1261
https://doi.org/10.1007/s11709-025-1210-7

RESEARCH ARTICLE

Wind-structure interaction data-driven neural-network model proposition for assessing performance of unique stiffening-helix against wind-induced open-top tank-buckling

Soumya MUKHERJEE[a,b*], Dilip Kumar SINGHA ROY[b]

[a] *Department of Civil Engineering, Indian Institute of Technology Palakkad, Palakkad 678623, India*
[b] *Department of Civil Engineering, National Institute of Technology Durgapur, Durgapur 713209, India*
[*] *Corresponding author. E-mail: mukherjee.s@iitpkd.ac.in*

ABSTRACT Empty steel-tanks are very much susceptible against buckling induced by wind loading. Ring and vertical stiffeners are commonly used to provide necessary strength to thin-walled steel tanks to resist wind-induced buckling. The authors have studied the performance of a unique, ribonucleic acid structure-inspired, stiffening-helix mechanism against the wind-induced buckling of open-top, cylindrical, empty, steel-tank. The most important output parameter of this study is the load multiplier (λ) of buckling, as it defines the stability of tank-shell against wind-induced buckling. The study variables are tank-height to tank-diameter (H/D) ratio, tank-radius to wall-thickness (r/t) ratio, basic wind speed (V_b) and helix pitch length to tank-height (L_P/H) ratio. This study has been performed through multiphysics system-coupling of computational fluid dynamics and structural mechanics (eigenvalue buckling). The stiffening-helix can provide necessary strength to open-top, cylindrical, steel-tank economically against wind-induced buckling. An artificial neural network (ANN) has been trained with the analytical data to develop a predictive model. The proposed predictive ANN model produces 99.11% average accuracy.

KEYWORDS open-top steel-tank, cylindrical steel-tank, stiffening-helix, wind-induced buckling, buckling load multiplier, artificial neural network

1 Introduction

The atmospheric wind harms an empty, cylindrical steel-tank by transverse wind load-induced bending and over-turning, oscillating wind flow-excited ovalling, and stagnation pressure-caused membrane force-induced buckling [1–5]. To protect the tank from overturning base of the tank is anchored by bolts or straps [6,7]. To minimize the bending and axial buckling of tank, vertical stiffener is useful and its performance can be improved with the application of corrugated shell course at the tank-wall [6,8]. Ring stiffener is applied to control the ovalling and circumferential buckling of tank wall [6,9]. Determination of the permissible height of unstiffened portion of shell and equivalent thickness of stepped wall from varying thickness of shell courses are important to assess the need of intermediate ring-stiffener [10,11]. Through simplified modeling of ring-stiffener through linear bifurcation, material and geometric nonlinear analyses using beam element with translational constraints can increase destabilization risk of tank by 7%, 12%, and 14% against thermal, wind and uniform loading [12]. But such modeling simplification does not alter the critical stress state of tank buckling significantly and can be faithful to the real scenario [13]. Top and intermediate ring stiffeners help in minimizing deformation at the tank's upper and intermediate portions, respectively [9]. The top stiffener is usually provided with greater size compared to the intermediate stiffener, but later studies highlight that similar size of both

Article history: Received Mar 14, 2025; Accepted May 8, 2025

stiffeners does not affect the tank's strength against buckling [14–18]. Modifications in the design formulae of permissible height of unstiffened shell-portion; moment of inertia, section modulus, radial shear, bending moment and stresses in both type of stiffener; internal spacing of intermediate stiffeners [19–22]. The concept of spiral stiffening of cylindrical shell under uniform torsion, compression and transverse loading, comes to light from the study of Yen [23] on the optimization of stiffener weight depending on the spiral angle. 30° angled spiral stiffener improves the response against axial buckling of ceramic shell on elastic Winkler foundation [24]. When spiral stiffener with spiral angle < 60° is attached at the inside face of the wall it reduces tank's capacity against thermal buckling compared to the externally connected spiral stiffener [25]. Higher resistance to thermal load induced large deflection can be seen in spirally stiffened functionally graded shell with damper, situated on elastic foundation, when the load is linearly varying, rather than uniform [26,27]. Through comparative study, Nam et al. [28] proved that spiral stiffener renders higher strength to shell against buckling, than orthogonal stiffener. Amalgamation of Von Karman's concept of nonlinearity with Donnel's shell-buckling theory forms the problem equations of the thermo-torsional buckling of shell with spiral stiffening mechanism based on Lekhnitskii's smeared stiffening approach, which can be solved with Galerkin method [29,30]. Exploring the applications of vertical, ring and spiral stiffeners it is evident that usage of ring stiffener is much more in practice for resisting wind-induced buckling damage and providing stability to cylindrical steel-tanks. Vertical stiffeners are applicable for resisting axial buckling of steel-tanks and less likely to be used against wind-induced buckling. Application of spiral stiffener is reported for the axial, thermal and torsional buckling of composite shells only and the performance of this type of stiffener is not tested or studied against wind-induced steel-tank buckling. This scope encouraged the authors to study the performance of stiffening-helix against the wind-induced tank buckling, which is inspired from the structure of ribonucleic acid (RNA). The study is performed by varying the tank's height to diameter (H/D) and radius to wall-thickness (r/t) ratio. The basic speed of wind (V_b) and pitch length of the stiffening-helix to tank height (L_p/H) ratio have also been varied in this study. The performance parameters are normalized radial deformation ($\delta_{r_{BN}}$) to assess damage and buckling load multiplier (λ) for understanding stability of tank. This study is not focused on providing designing specification for the stiffening-helix and American petroleum institute (API) 650 [31] guidelines is applied to calculate the section modulus of the stiffening-helix as intermediate stiffener. The wind-structure interaction (WSI) has been studied with the help of Ansys multiphysics-based system coupling of CFX solver for the computational fluid dynamics (CFD) modeling of wind flow and mechanical solver for eigenvalue buckling analysis of tank with the imported wind pressure data from CFD [32,33].

Experimentations and high-end analytical studies on the stiffener performance against wind-induced tank buckling need costly testing, sensor and high-performance computing setup along with significant amount of time. There is a severe scarcity of studies exploring the application of machine learning models for assessing wind pressure variation and buckling of cylindrical thin-walled shell. Gradient boosting regression tree model is found to be efficient for forecasting average aerodynamic pressure and its fluctuation on isolated shells based on their geometric variation, whereas artificial neural network (ANN) model is proved to be effective for the prediction of similar aerodynamic parameters when an elevated cylindrical shell is facing wind-interference scenario due to a nearby building [34,35]. Existing machine learning based studies, which are focused on the shell-buckling, have considered the buckling effect due to axial compressive load, unlike wind pressure induced membrane stress created buckling of thin-walled tank-shell [36–40]. Samaniego et al. [41] and Mishra et al. [42] implemented neural network for solving partial differential equations of linear elastic and nonlinear transient elasto-dynamics problems, which is an efficient amalgamation of computational mechanics and machine learning. These literatures on machine learning applications explores the aerodynamic pressure characteristics and buckling of cylindrical shell in a separate manner. An absence of study focusing on the machine learning model of wind-induced buckling of thin-walled shell is noticed. The authors have also taken up this scope and introduced a novel ANN model which is trained with the data obtained from the WSI analyses of wind-induced buckling of open-top tank strengthened with stiffening-helix. Several analytical parameters are associated with this study, of which the nomenclatures are enlisted in Table 1.

2 Novelty statement

Wind-induced buckling of large diametric circular steel storage is a fairly under studied area of research. This study provides a fresh approach of addressing this real-life issue of wind-induced buckling damage or failure of such steel-storages, especially tanks, both in terms of innovative stiffening mechanism and procurement of machine learning model for time-economic and easier design of these structures. Importance has been provided to nondimensional parametric study so that generalized understanding can be achieved on the performance of a unique RNA-inspired stiffening-helix to stabilize open-

Table 1 Nomenclature

Symbol	Description	Symbol	Description
a	output of neural network	a_l	neural network output for lth data set
b	bias	C_{pe}	external wind pressure coefficient
C_{pi}	internal wind pressure coefficient	$C_{\mathrm{pe}_{\mathrm{mean}}}$	mean external wind pressure coefficient
$C_{\mathrm{pi}_{\mathrm{mean}}}$	mean internal wind pressure coefficient	D	tank diameter
f_{i}	body force induced mean stress	F_{y}	yield strength
G	gust factor	G_{k}	mean velocity gradient induced kinetic energy
H	tank height	H_{TI}	height between top and intermediate ring
I	importance factor	I_{z}	turbulence intensity at elevation z
j_{e}	location number of external pressure tap	j_{i}	location number of internal pressure tap
k	turbulence kinetic energy	K_{d}	wind directionality factor
K_{T}	tangent stiffness matrix	K_{z}	exposure coefficient
K_{zt}	topography factor	l	data set number
L_{P}	pitch length of stiffening-helix	m	mode number
MSE	mean squared error	m	mode number
N	total number of time samples	p	mean pressure induced isotropic stress
P	equivalent wind pressure	P_{B}	buckling stress
P_{H}	free stream pressure at height H	p_{i}	input
P_j	wind pressure at tapping point	$P_{j_{\mathrm{e}}}$	wind pressure at external pressure tap
$P_{j_{\mathrm{i}}}$	wind pressure at internal pressure tap	p_{l}	number of inputs
P_{M_n}	measured wind pressure at nth tapping point	P_{U}	uniform pressure induced stress
P_{wd}	design wind pressure	P_{wv}	design wind velocity pressure
$P_{z_{\mathrm{ref}}}$	wind pressure at reference elevation z_{ref}	P_η	incremental stress of ηth load function
r	tank radius	R	correlation coefficient
S	modulus of strain tensor	S_{ij}	average rate of strain tensor
S_{S}	stress stiffening matrix	t	wall thickness
T	time	t_{l}	number of target output
U_{H}	wind speed at height H	u_i	mean velocity component along ith spatial coordinate x_i
u_j	mean velocity component along jth spatial coordinate x_j	u_i'	fluctuating velocity component along ith spatial coordinate x_i
u_j'	fluctuating velocity component along jth spatial coordinate x_j	U_{z}	wind speed at height z
$U_{z_{\mathrm{ref}}}$	wind speed at reference elevation z_{ref}	V	design speed of gust
V_{b}	basic wind speed	W	weight
y	sigmoid function	z	vertical axis
z_{G}	gradient height of atmospheric boundary	α	power law coefficient
$\delta_{r_{\mathrm{B}}}$	buckling induced radial deformation	δ_{r_η}	incremental radial deformation
$\delta_{r_{\mathrm{U}}}$	uniform pressure induced radial deformation	ε	dissipated energy of turbulent flow
Φ	circumferential axis	ψ	eigen vector
λ	buckling load multiplier	μ	dynamic viscosities
μ_{t}	turbulence viscosity	η	total number of load functions
n	number of neurons	η	number of training data set
ρ	density of air	θ	circumferential angle
ζ	nondimensional vertical axis	ν	kinematic viscosities
ω_{k}	angular speed	$\bar{\Omega}_{ij}$	mean rate of rotation tensor

top, ground-supported, cylindrical, steel-tank against wind-induced buckling. This study also addresses the lack of machine learning model for assessing wind-induced shell buckling. An ANN-based prediction model has been introduced for predicting the stability of open-top, cylindrical steel-tank against wind-induced buckling. The proposed stiffening-helix mechanism provides satisfactory stabilization to the tank against wind-induced buckling. Also, the reported accuracy of the predictive ANN model signifies that this model can be used by structural engineers for the safe design of open-top, cylindrical steel-tank against wind-induced buckling.

3 Description of the computational fluid dynamics modeling

3.1 Specifications of virtual model and domain

Bluff body analysis through CFD modeling has been performed to assess the wind pressure. Open top, ground-supported tank model with 20 m diameter (D) has been considered as the bluff body, whose height (H) was varied in a range of 5 to 20 m with 5 m interval, representing for four different H/D ratios (0.25, 0.5, 0.75, and 1.0). The virtual wind domain has been shaped to maintain 3% to 5% blockage ratio, according to the recommendations of architectural institute of Japan (AIJ) [43]. The opening for letting the wind flow in the domain, the domain-roof and walls on the domain-sides are five times the maximum tank dimension (H or D whichever is applicable) apart from the corresponding face of model. The distance between respective model surface and wind outflow opening of the domain is 15 times the extreme dimension of the tank, which provides sufficient space to the vortices generating behind the model, thus avoiding any chance of flow recirculation. Free slip side wall and roof surfaces of the domain do not affect the wind flow. Smooth base of domain and faces of tank represents the surface roughness necessary for open terrain and minimizes the creation of small near-wall vortices around the model, respectively. The schematic diagram of domain showing the dimensions is provided in Fig. 1.

3.2 Approach of turbulence modeling

The turbulence modeling of the wind flow has been carried out through Ansys CFX [32]. Despite the reputation of large eddy simulation (LES) model in replicating precise near wall vortices around complex building structures, three-dimensional (3D) unsteady Reynolds averaged Navier Stokes (URANS) model has been applied in this study, as it is fairly accurate and time saving way of simulating sub-grid to large scale vortices around structures with simple geometry like cylindrical tank [44–51]. The formulations of continuity and momentum for 3D URANS turbulence model are provided in Eqs. (1) and (2), which are solved by Reynolds decomposition of incompressible wind flow into fluctuating and time-averaged components [52]. Due to the less accuracy of standard k–ε model, realizable k–ε model has been applied as eddy-viscosity model to define the separation of rotational wind flow's boundary layer with the expressions of kinetic (k) and dissipated (ε) energies as Eqs. (3) and (4), caused by energy transfer during turbulence in flow [53, 54]. The mean momentum-shift for URANS model, caused by the unsteady convection of flow, is expressed with mean pressure (p) induced isotropic stress, dynamic viscous stress, body force induced mean stress (f_i) and Reynolds stress due to fluctuating velocity components u_i' and u_j' along ith and jth spatial coordinates. Equational coefficient C_1 of dissipated energy is calculated as Eq. (5). Mean velocity gradient induced kinetic energy (G_k), presented in Eq. (6), is composed of modulus of strain tensor (S) and turbulence viscosity (μ_t), which are showed in Eqs. (7) and (8), respectively. Various equation components C_μ, A_s, $\tilde{\Omega}_{ij}$, ϕ, and $\tilde{S}$, are subsequently provided as Eqs. (9)–(13). Average rate of strain tensor (S_{ij}) is showcased as Eq. (14). Density of air, mean rate of rotation tensor, angular speed, kinematic and dynamic viscosities are presented as ρ, $\bar{\Omega}_{ij}$, ω_k, ν, and μ. u_i and u_j are mean components of velocity along x_i and x_j. The value of the constants σ_k, C_2, A_0, and σ_ε are 1.0, 1.9, 4.04, and 1.2, accordingly.

$$\frac{\partial u_i}{\partial x_i} = 0, \tag{1}$$

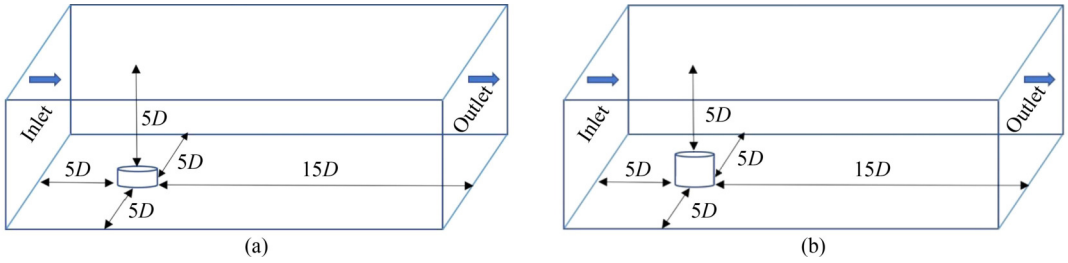

Fig. 1 Dimensional diagram of domain in cases of tank H/D ratio: (a) < 1.0; (b) 1.0.

$$\frac{\partial}{\partial t}(\rho u_i)+\frac{\partial}{\partial x_j}(\rho u_i u_j)=-\frac{\partial p}{\partial x_i}+\frac{\partial}{\partial x_j}(\mu+\mu_t)\left(\frac{\partial u_i}{\partial x_j}+\frac{\partial u_j}{\partial x_i}\right), \tag{2}$$

$$\frac{\partial}{\partial t}(\rho k)+\frac{\partial}{\partial x_j}(\rho k u_j)=\frac{\partial}{\partial x_j}\left[\left(\mu+\frac{\mu_t}{\sigma_k}\right)\left(\frac{\partial k}{\partial x_j}\right)\right]+G_k-\rho\varepsilon, \tag{3}$$

$$\frac{\partial}{\partial t}(\rho\varepsilon)+\frac{\partial}{\partial x_i}(\rho\varepsilon u_i)=\frac{\partial}{\partial x_j}\left[\left(\mu+\frac{\mu_t}{\sigma_\varepsilon}\right)\left(\frac{\partial \varepsilon}{\partial x_j}\right)\right]+\rho C_1 S\varepsilon - \rho C_2\left(\frac{\varepsilon^2}{k+\sqrt{\nu\varepsilon}}\right), \tag{4}$$

$$C_1=\max\left[0.43,\frac{Sk/\varepsilon}{Sk/\varepsilon+5}\right], \tag{5}$$

$$G_k=\mu_t S^2, \tag{6}$$

$$S\equiv\sqrt{2S_{ij}S_{ij}}, \tag{7}$$

$$\mu_t=\rho C_\mu\frac{k^2}{\varepsilon}, \tag{8}$$

$$C_\mu=\frac{1}{A_0+A_s\dfrac{k\sqrt{S_{ij}S_{ij}+\tilde{\Omega}_{ij}\tilde{\Omega}_{ij}}}{\varepsilon}}, \tag{9}$$

$$A_s=\sqrt{6}\cos\phi, \tag{10}$$

$$\tilde{\Omega}_{ij}=\bar{\Omega}_{ij}-3\varepsilon_{ijk}\omega_k, \tag{11}$$

$$\phi=\frac{1}{3}\cos^{-1}\left(\sqrt{6}\frac{S_{ij},S_{jk},S_{ki}}{\tilde{S}^3}\right), \tag{12}$$

$$\tilde{S}=\sqrt{S_{ij}S_{ij}}, \tag{13}$$

$$S_{ij}=\frac{1}{2}\left(\frac{\partial u_j}{\partial x_i}+\frac{\partial u_i}{\partial x_j}\right). \tag{14}$$

3.3 Details of time history analysis and calculation of pressure coefficient

Time history analysis has been performed to assess the aerodynamic pressure of 3.0 s gust duration as per IS 875-2015, part 3 [55], through second order backward Euler method with the converging target value of root mean square (*RMS*) residual as 0.00001 [56]. The iterative transient analysis has been carried out with 0.001 s time stepping and maximum 10 numbers of iterative cycles at each step, as per AIJ guidelines [43]. Following the works of Portela and Godoy [57] the external (C_{pe}) and internal (C_{pi}) coefficients of wind pressure have been assessed with Eqs. (15) and (16). P_{j_e} and P_{j_i} represents the wind pressure measured from circumferential pressure taps on external (j_e) and internal (j_i) surfaces of tank-wall. The pressure taps are located circumferentially on the inside and outside faces of tank-wall at elevations 0.25H, 0.5H, and 0.75H. The tapping point pressure P_j is generally expressed as Eq. (17) as circumferential angle (θ) and time (T) dependent function of measured pressure (P_{M_n}) at nth tapping point. As per the study of Bairagi and Dalui [58], the free stream pressure (P_H) of wind at similar elevation to the tank top is presented as Eq. (18), considering the wind speed as U_H at an elevation equivalent to the tank top. The time-averaged pressure coefficients at the exterior ($C_{pe_{mean}}$) and interior ($C_{pi_{mean}}$) surfaces of tank-wall are calculated as Eqs. (19) and (20), from pressure data of N number of time instances.

$$C_{pe}=\frac{P_{j_e}}{P_H}, \tag{15}$$

$$C_{pi}=\frac{P_{j_i}}{P_H}, \tag{16}$$

$$P_j=P_{M_n}(\theta,T), \tag{17}$$

$$P_H=0.5\rho U_H^2, \tag{18}$$

$$C_{pe_{mean}}=\frac{1}{N}\sum_{j_e=n-1}^{j_e=n}C_{pe}(T), \tag{19}$$

$$C_{pi_{mean}}=\frac{1}{N}\sum_{j_i=n-1}^{j_i=n}C_{pi}(T). \tag{20}$$

3.4 Validation of computational fluid dynamics model with experimental literature with the help of mesh sensitivity analysis

The present CFD model was already validated with the help of sensitivity analysis of the mesh, in the previous study by the authors, Mukherjee et al. [35], with respect to the wind tunnel test output of Portela and Godoy [59], which is explained in this section. In the studies of Mukherjee et al. [35] full scale tank's H/D ratio (D = 20 m, and H = 8.75 m) was similar to the scaled model (D = 269.2 mm, and H = 115.7 mm) of Portela and

Godoy [59] for wind tunnel test. The basic wind speed in the study of Mukherjee et al. [35] has been taken as 64.8 m/s, which was similar to the scaled speed 19.8 m/s at 116 mm inside wind tunnel test section of the study of Portela and Godoy [59]. The terrain was open terrain for both studies [35,59]. Tetrahedral mesh with inflation at corners and edges for ensuring precise flow separation, has been used for discretization as per the studies of Franke et al. [60]. To determine the optimum sizing of mesh, Mukherjee et al. [35] applied three different meshing sizes, namely fine mesh (FM), medium mesh (MM) and coarse mesh (CM), of which the images and specifications are provided in Table 2 and Fig. 2, respectively. Mukherjee et al. [35] compared the external pressure coefficients in Fig. 3(a), obtained from the CFD analyses using the three different mesh sizes, with the same from the experimentation of Portela and Godoy [59]. Similar pressure reporting elevation (0.6*H*) like the study of Portela and Godoy [59], has been considered by Mukherjee et al. [35]. The percentages of error in pressure coefficient are 3.21%, 14.23%, and 36.63%, accordingly, for FM, MM, and CM mesh sizes in comparison to Portela and Godoy [59], which is shown in Fig. 3(b). The FM with the least percentage of error has been determined for the optimum requirement for the mesh sizing. The model and domain have been discretized with the FM, which is exhibited in Fig. 4.

3.5 Theoretical validation of computational fluid dynamics model with velocity and turbulence intensity profiles

The theoretical validation was also performed by the authors, Mukherjee et al. [35] in the previous study by comparing wind velocity and turbulence intensity profiles obtained from the CFD model with the theoretical model using power law, as per AIJ [43]. The power laws of wind velocity and turbulence intensity are expressed as Eqs. (21) and (22), in which U_z and I_z are wind speed and turbulence intensity at elevation z, $U_{z_{ref}}$ is the reference wind speed at reference elevation z_{ref}, z_G is gradient height of atmospheric boundary and α is coefficient of power law. The study has been performed considering

Table 2 Details of different meshes

Mesh type	Node number	Element number	Edge length ratio	Element volume ratio	Curvature angle	Skewness
FM	16753678	77606245	⩽ 80.43	⩽ 91.67	18°	⩽ 0.90
MM	14682539	73592159	⩽ 85.71	⩽ 96.32	24°	⩽ 0.95
CM	12323547	57937626	⩽ 107.92	⩽ 111.54	73°	⩽ 1.00

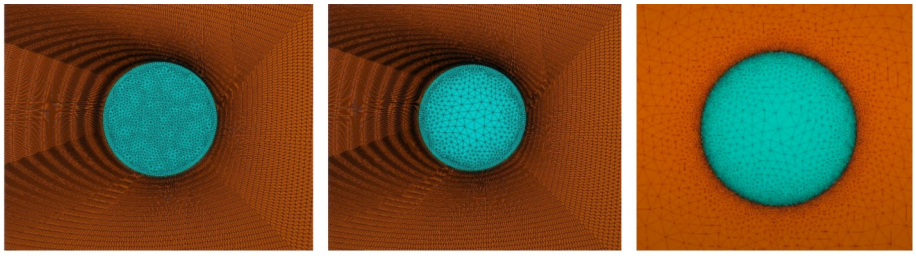

(a) (b) (c)

Fig. 2 Images of mesh: (a) FM; (b) MM; (c) CM.

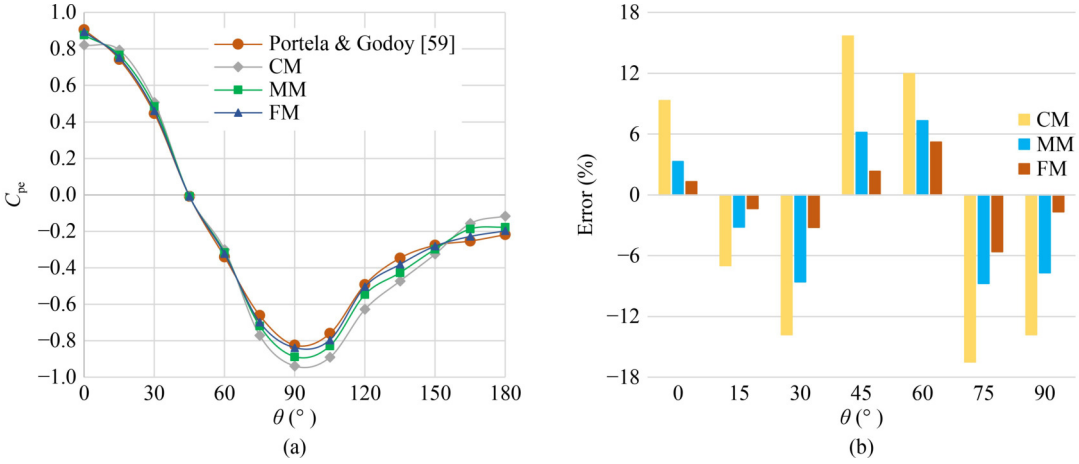

Fig. 3 Comparison of: (a) pressure coefficients; (b) percentage of error.

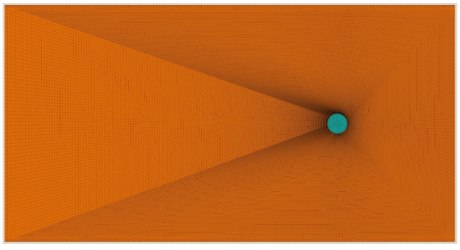

Fig. 4 Mesh of domain.

open terrain condition in Indian subcontinent, consequently α and z_G have been taken as 0.188 and 300 m as per IS 875-2015, part 3 [55] and IS SP 64-2001 [61]. The reference wind speed has been considered as 50 m/s at 10 m. The reference turbulence intensity at gradient height has been considered as 1% for CFD model. The comparison of CFD and theoretical profiles for wind velocity and turbulence intensity, taken at 4D distance from the tank as per AIJ [43], is showcased in Figs. 5(a) and 5(b), accordingly. Theoretical and CFD profiles of wind speed are nearly similar, whereas some variation is observed for turbulence intensity. Although the variation for turbulence intensity is < 10% upto the elevation similar to the tank's height, which will not affect the wind pressure distribution pattern in a significant manner. For the present study purpose eight different basic speed of wind has been considered, which are 5, 15, 25, 35, 45, 55, 65, and 75 m/s.

$$U_z = U_{z_{ref}}\left(\frac{z}{z_{ref}}\right)^{\alpha}, \tag{21}$$

$$I_z = 0.1\left(\frac{z}{z_G}\right)^{-\alpha-0.005}. \tag{22}$$

4 Analogy of wind pressure induced-buckling

4.1 Structural details

Bluff body analyses have been performed through CFD model for eight different basic wind speeds and four various H/D ratios of open-top, cylindrical, steel tank. Six various r/t ratios, which are 750, 1000, 1250, 1500, 1750, and 2000, have been used during the structural modeling of the tanks. The tank-base and top have been considered as fixed and free, respectively. A unique RNA inspired stiffening-helix has been applied as intermediate stiffener along with ring-stiffeners at the top of tank and bottom end of the stiffening-helix. The pitch length (L_p) of the stiffening-helix has been varied four times, which are $H/5$, $4H/15$, $2H/5$, and $4H/5$. The diagram of the tank with H/D ratio 0.5 is provided in Fig. 6, showcasing all the details of stiffening-helix pitch length. The section modulus (Z_{TR}) of the top wind girder has been designed as the top ring-stiffener design guidelines following API 650 [31], which is shown in Eq. (23). Whereas the stiffening-helix and bottom ring-stiffener section moduli (Z_{IR}) have been designed as per the intermediate ring-stiffener design method of API 650 [31], which is presented as Eq. (24). The stiffener's lowest yield strength (F_y) requires to be the smaller value between 210 MPa and strength at peak working temperature (in MPa). The design pressure of wind is P_{wd} (kPa), expressed as Eq. (25). The design velocity pressure of wind (P_{wv}) at 10 m elevation and basic pressure (p) have been presented as Eqs. (26) and (27), subsequently. The coefficient of exposure of the pressure of velocity (K_z) is 1.04, the factor of gust (G) is 0.85, the design speed of gust (V) is 190 km/h at 10 m height, the circular tank's directionality

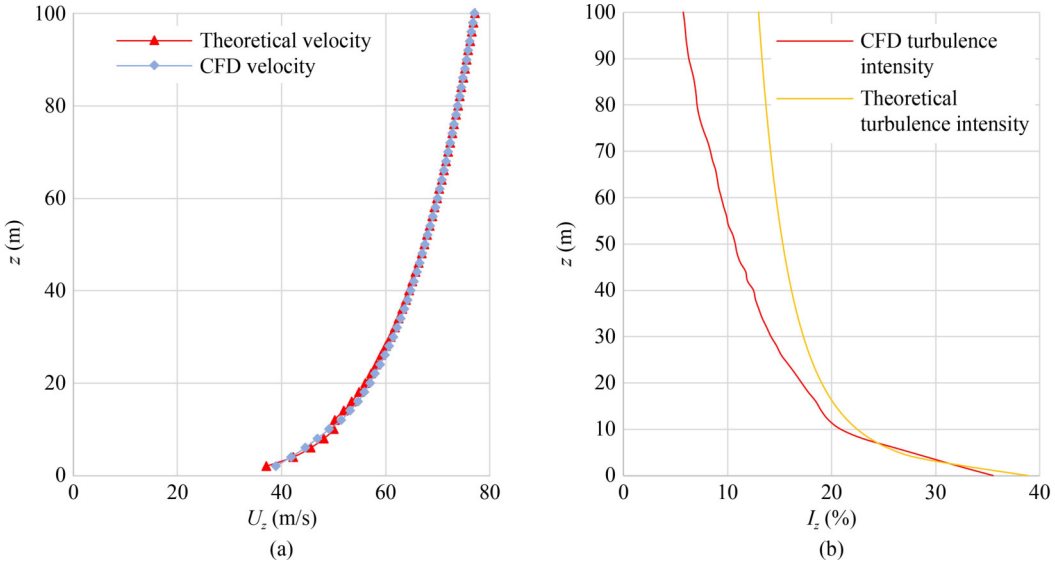

Fig. 5 Distributions of: (a) velocity; (b) intensity of turbulence with the elevation.

factor of wind (K_d) is 0.95, the factor of structural importance (I) is 1.0 and the topographical factor (K_{zt}) is 1.0.

$$Z_{TR} = \frac{6HD^2}{0.5F_y}\left(\frac{P_{wd}}{1.72}\right), \tag{23}$$

$$Z_{IR} = \frac{6H_{TI}D^2}{0.5F_y}\left(\frac{P_{wd}}{1.72}\right), \tag{24}$$

$$P_{wd} = P_{wv} + 0.24, \tag{25}$$

$$P_{wv} = p\left(\frac{V_b}{190}\right)^2, \tag{26}$$

$$p = 0.00256K_zK_{zt}K_dV^2IG. \tag{27}$$

4.2 Element details

Cylindrical steel tank is a thin-walled shell structure, for this reason the tank wall has been discretized with two dimensional (2D) SHELL181 element, which has 4 nodes, each having six degrees of freedom (DOF) [62]. The stiffening-helix and other stiffeners have been meshed with BEAM188 element with two nodes having six DOF each [62]. The stiffener needs to be attached with the steel tank with welded connection as per API 650 [31] and IS 803-1976 [63]. The welded connection between stiffener and tank has been replicated by applying CONTA175 element, as bonded contact with zero penetration using Lagrangian formulation [64–67]. The contact region mesh between tank and stiffeners is shown in Fig. 7. The wind pressure from CFD solver has been imported to the mechanical solver and transformed into an asymmetrical surface pressure on the wall of tank by applying SURF154 element with four to eight nodes with three DOF at each node [68]. Similar to the previous study of the authors, Mukherjee et al. [69], 50 mm element size has been used for the wind-induced buckling analysis according to the study of Sun et al. [70], which proposes that the circular tank's circumference needs to be minimum 1256 times greater than the element size.

4.3 Analytical details

The authors have analyzed the wind-pressure induced buckling of the tank by transforming the wind pressure into an equivalent non-uniform surface pressure, similar to the previous study of the authors, Mukherjee et al. [69,71]. This transformation technique of the wind pressure as arbitrarily distributed surface pressure is inspired from the analytical model of Yang et al. [72,73]. Considering cylindrical coordinate system for cylindrical tank, the surface wind pressure has been decomposed into axial and circumferential pressure components $P(z)$ and $P(\Phi)$, respectively, where z and Φ are axial and circumferential axes. The representation of circumferential axis in terms of radius (r) of tank-shell and circumferential angle (θ) is expressed as Eq. (28). The wind pressure as functions of elevation (z) and circumferential angle (θ) are shown as Eqs. (29) and (30). Non-dimensional equation parameters are β_1, β_2, and ϵ $(0 \leqslant \epsilon \leqslant 1)$. The reference pressure ($P_{z_{ref}}$) has been considered as the velocity pressure of wind at the stagnation zone following the study of Yasunaga and Uematsu [74]. In case of analyzing wind-induced nonlinear oscillation of stiffened shell, the eigenvalue problem of the stiffener's stiffness

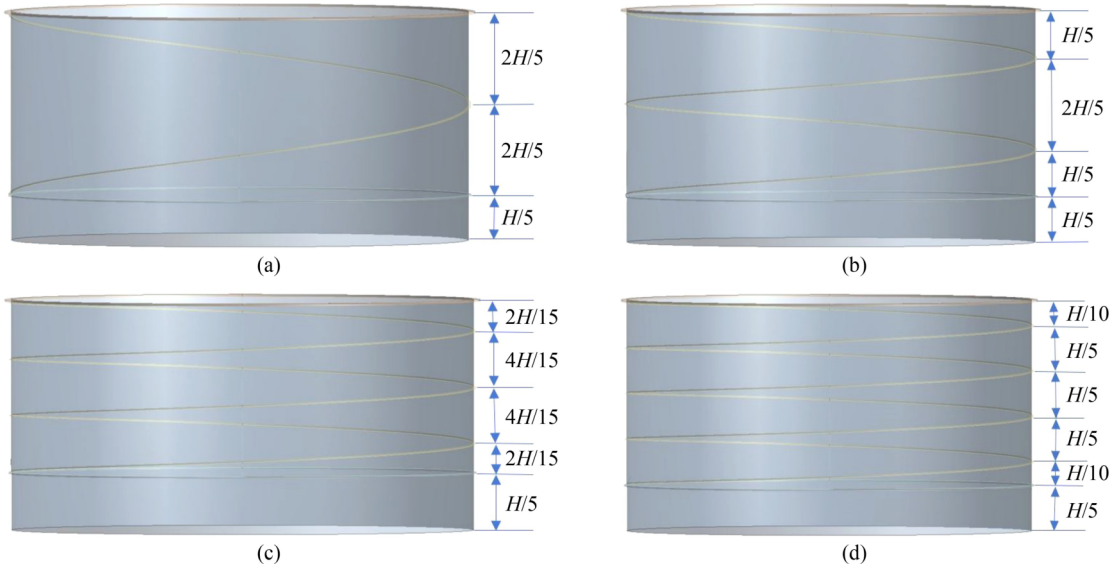

Fig. 6 Mesh of tank model having H/D ratio 0.5 with helical stiffener's turn number: (a) 1; (b) 2; (c) 3; (d) 4.

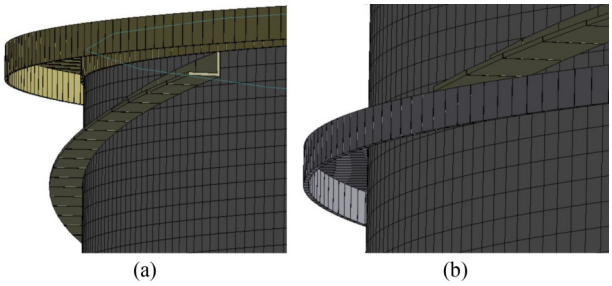

Fig. 7 The mesh for connection of helical stiffener with: (a) top; (b) bottom wind girder.

can be computed by eliminating nonlinear terms of Timoshenko-Ehrenfest beam theory [75]. But, in present analytical approach for wind-induced shell buckling, the buckling stress (P_B) has been formulated through Eq. (31), as the sum of the uniform pressure induced stress (P_U) and the total of all the incremental stresses (P_η) upto ηth load function. The circumferential compression of the tank-wall creating membrane stress is similar to the behavior of Mindlin-Reissner plate under time-modulated axial force, which in turn produces the circumferential waves of wind-induced buckling [76]. Summation of uniform pressure induced radial deformation (δ_{r_U}) and incremental radial deformations (δ_{r_η}) caused by the total number (η) of load functions express the buckling induced radial deformation (δ_{r_B}) through Eq. (32). The nondimensional longitudinal axis (ζ) of the cylindrical coordinate system is represented as z/H ratio. The load multiplier (λ) of buckling is expressed as Eq. (33). The governing formulation of eigenvalue buckling analysis is provided in Eq. (34) [33]. Where, stress stiffening matrix, tangent stiffness matrix, buckling load multiplier and eigen vector at mth mode are S_S, K_T, λ_m, and ψ_m.

$$\Phi = r\theta, \tag{28}$$

$$P(z) = P_{Z_{ref}}\left[1+\epsilon\left(\frac{z}{H}+\frac{1}{2}\right)\right], \tag{29}$$

$$P(\theta) = P_{Z_{ref}}\left[1+\beta_1+\epsilon\beta_1(\cos\theta-1)+\epsilon\beta_2(\cos 2\theta)\right], \tag{30}$$

$$P_B = P_U + \sum_{\eta=1}^{\infty}\epsilon^\eta P_\eta, \tag{31}$$

$$\delta_{r_B}(\zeta,\theta) = \delta_{r_U} + \sum_{\eta=1}^{\infty}\epsilon^\eta \delta_{r_\eta}(\zeta,\theta), \tag{32}$$

$$\lambda = \frac{P_B}{P(z,\phi)}, \tag{33}$$

$$[K_T + \lambda_m[S_S]]\{\psi_m\} = \{0\}. \tag{34}$$

5 Supervised training of artificial neural network

5.1 Details of network architecture

Application of ANN for the predictive modeling of shell buckling is limited to the effect of axial compression [36]. The authors have introduced a novel feed-forward backpropagation ANN model for prediction of tank stability against wind pressure-induced buckling through training with the WSI data. Similar to the physical nervous system with neurons, the ANN consists of computational units called neuron. Similar to the information receiving, transfer, process and command delivering mechanism of physical nervous system, ANN receives the data as input, transfers through hidden layers, processes with neurons and delivers the computational result as output. The input variables of present study are H/D, r/t, L_P/H, and V_b (m/s) to assess the stability of tank against wind-induced buckling in terms of load multiplier (λ) of buckling as output. Neural network can be improvised with particle swarm optimization or devised with higher number of hidden layers and neurons to assess highly nonlinear and complex shell buckling with multi-input and multi-output [77]. But when the data complexity is relatively less with single output, single hidden layer can be sufficient, which is also applied in present study [78]. To finalize the optimum neuron requirement, variations have been carried out in the neuron number from ten to 40. The architecture of ANN model is provided in Fig. 8, where $\hat{n}$ is the neuron number.

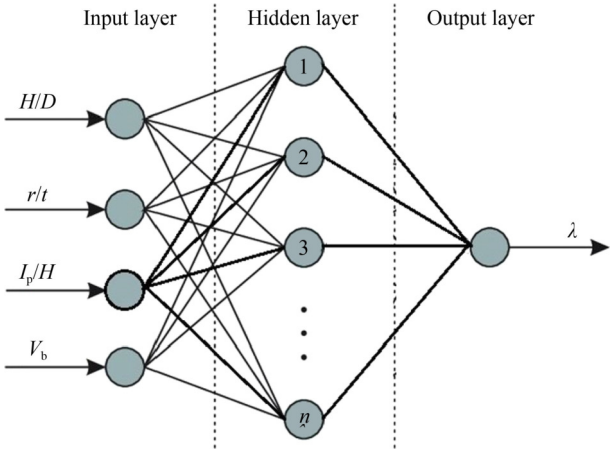

Fig. 8 Basic architecture of ANN in present study.

5.2 Performance assessing parameters of the network

Similar to the previous study of Mukherjee et al. [35], the authors used regression or correlation coefficient (R) and mean squared error (MSE) as the performance assessing parameters for the ANN model, which are shown in

Eqs. (35) and (36). The regression value ranges from −1.0 to 1.0. R value closer to 1.0 shows the higher precision level of correlation performance. In case of *MSE* value, the smaller the better in terms of accuracy and minimization of error. The number of training data set, the target output and ANN output of the lth data set are η, t_l and a_l. For the activation purpose the sigmoid function has been used, which is provided in Eq. (37). The output of ANN has been expressed as a function of input p_i, weight W and bias b, which is shown in Eq. (38). The weight matrix (W) is expressed as Eq. (39), where number of neuron and input are represented as $\underset{\sim}{\eta}$ and p_l, respectively. Due to the adaptability, quick convergence and optimum efficiency, Levenberg–Marquardt (LM) training function has been applied for the data training [57,79]. The training parameters of LM algorithm are adjustment parameter (*mu*), maximum value (*mu_max*), increment factor (*mu_inc*) and decrement factor (*mu_dec*) of adjustment parameter by Marquardt. When the gradient is less than minimum gradient (*min_grad*) or failure number of validation is more than maximum failure number in validation (*max_fail*), the training gets stopped.

$$R = \sqrt{1 - \frac{\sum_{l=1}^{\eta} (t_l - a_l)^2}{\sum_{l=1}^{\eta} (t_l - \bar{t}_l)^2}}, \tag{35}$$

$$MSE = \frac{1}{\eta} \sum_{l=1}^{\eta} (t_l - a_l)^2, \tag{36}$$

$$y = \frac{2}{1 + \mathrm{e}^{-2x}} - 1, \tag{37}$$

$$a = f(Wp_i + b), \tag{38}$$

$$W = \begin{bmatrix} w_{1,1} & w_{1,2} & \cdots & w_{1,p_l} \\ w_{2,1} & w_{2,2} & \cdots & w_{2,p_l} \\ \cdots & \cdots & \cdots & \cdots \\ w_{\underset{\sim}{\eta},1} & w_{\underset{\sim}{\eta},2} & \cdots & w_{\underset{\sim}{\eta},p_l} \end{bmatrix}. \tag{39}$$

6 Results and discussions

6.1 Wind-induced buckling

The circumferential distribution of mean pressure coefficients of wind on external and internal surfaces of tank-wall, which are calculated from the CFD analyses, are expressed graphically from Figs. 9(a)–9(d), for tank's H/D ratio 0.25 to 1.0, accordingly. Positive wind pressure and suction are observed at the frontal region and side to leeward zone, respectively. The positive pressure and suction at the external wall-surface rises with the incremental pattern of the ratios of H/D and tapping elevation (z) to tank height (H). The internal suction subsequently decreases and increases with the rise in z/H and H/D ratios. In the earlier studies, the authors described the wind-induced buckling mechanism of open-top steel-tank [69,71]. The membrane stresses occur in the tank-wall and propagate through the sides of the tank before meeting at the frontal zone due to the peripheral distribution of aerodynamic pressure, which creates circumferential buckling waves at the frontal region's wall. The distribution of wind pressure and consequent buckling waves are exhibited schematically in Figs. 10(a) and 10(b), respectively. The radial deformations of the tanks for the considered cases of wind-induced buckling have been analyzed. The radial deformation helps to assess the damaged portion of the tank-wall due to the buckling waves caused by wind-induced membrane stress. The radial deformation has been normalized with respect to the maximum value. The normalized radial deformation contours for tanks with four different H/D ratios are presented in Figs. 11(a)–11(d). The outward and inward radial deformations have been regarded as positive and negative, accordingly in the contour, which is shown in the color legend. The $\delta_{r_{BN}}$ contour exhibits presence of buckling waves at the wind-ward region of the tank wall. The number and amplitude of the buckling waves respectively rises and minimizes with the decrement in the L_P/H ratio of the stiffening-helix. Greater slenderness ratio of the tank shows larger amplitude and number of buckling waves. It is observed that for a particular H/D ratio of the tank with stiffening-helix having a certain L_P/H ratio, the resulting normalized radial deformation ($\delta_{r_{BN}}$) of tank-wall and number of buckling waves due to wind-induced buckling, is nearly identical in all the combinations of wind speed and wall-thickness cases. This observation signifies that although normalized radial deformation is useful for damage assessment, it is not a reliable parameter of tank's stability against wind-induced buckling.

The buckling load multiplier (λ) for all the cases of open-top steel tanks with stiffening-helix, have also been analyzed, which are presented in Fig. 12. Different values of load multiplier for each case of wind-induced tank-buckling signifies that the buckling load multiplier is a reliable parameter to assess the stability of a tank. Consequently, analysis of load multiplier is a way of understanding the performance of stiffening-helix against wind-induced tank buckling. The multiplier of buckling load reduces by 2.54%, 2.23%, 2.63%, 2.04%, 1.78%, 1.53%, and 6.6% with the gradual rise in basic wind speed from 5 to 75 m/s. With the decrease in L_P/H ratio

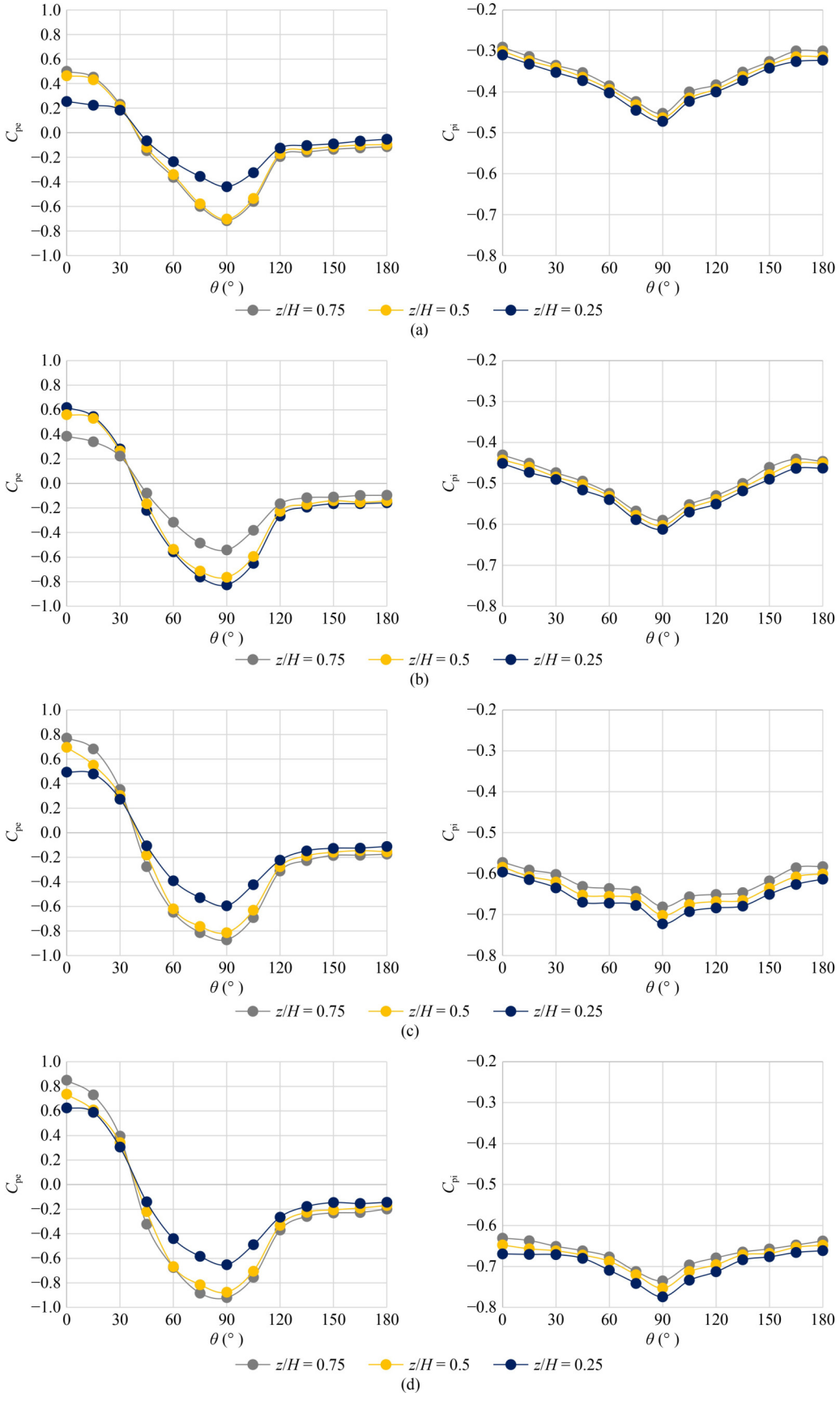

Fig. 9 Mean coefficients of aerodynamic pressure on exterior and interior wall-surfaces for open-top tank H/D ratio: (a) 0.25; (b) 0.5; (c) 0.75; (d) 1.0.

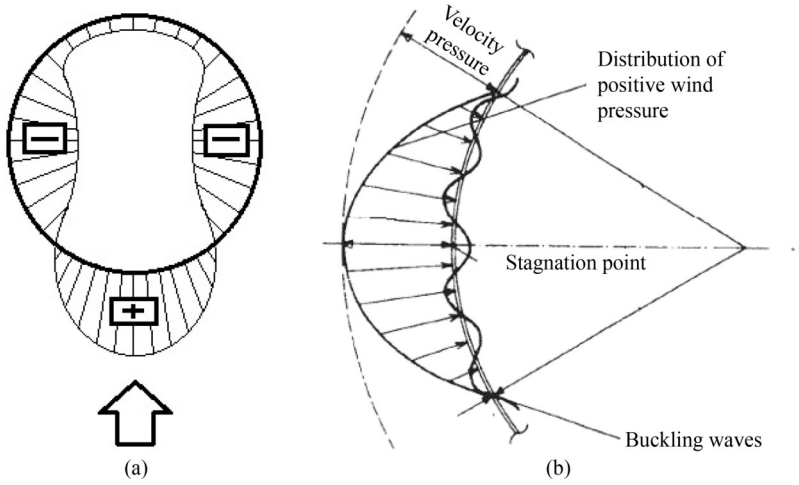

Fig. 10 Diagrams for the patterns of: (a) pressure of wind; (b) wind-induced buckling wave.

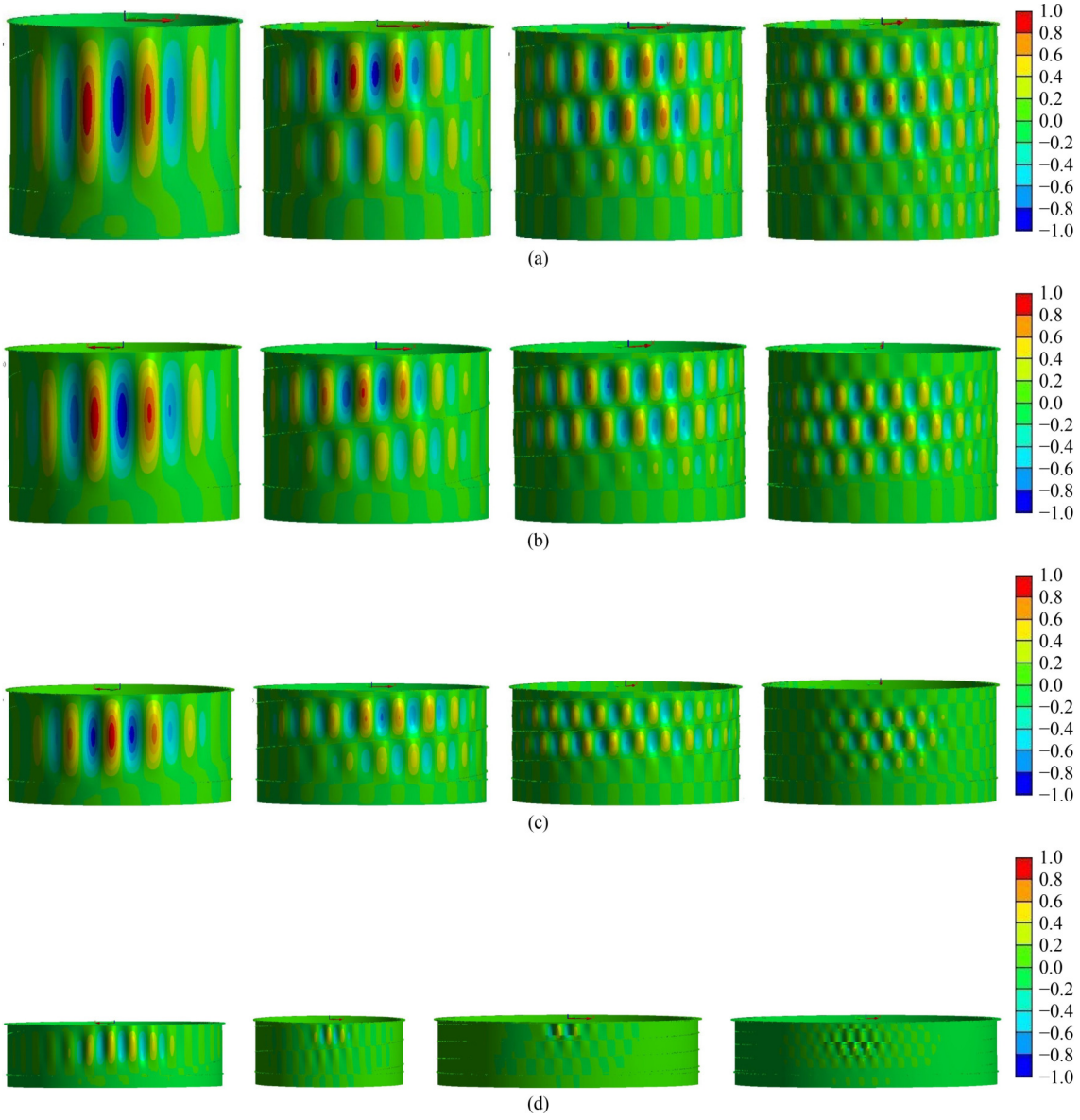

Fig. 11 Effect of L_P/H ratio of stiffening-helix on $\delta_{r_{BN}}$ of open-top, helically-stiffened, ground-supported tank for H/D ratio: (a) 1.0; (b) 0.75; (c) 0.5; (d) 0.25.

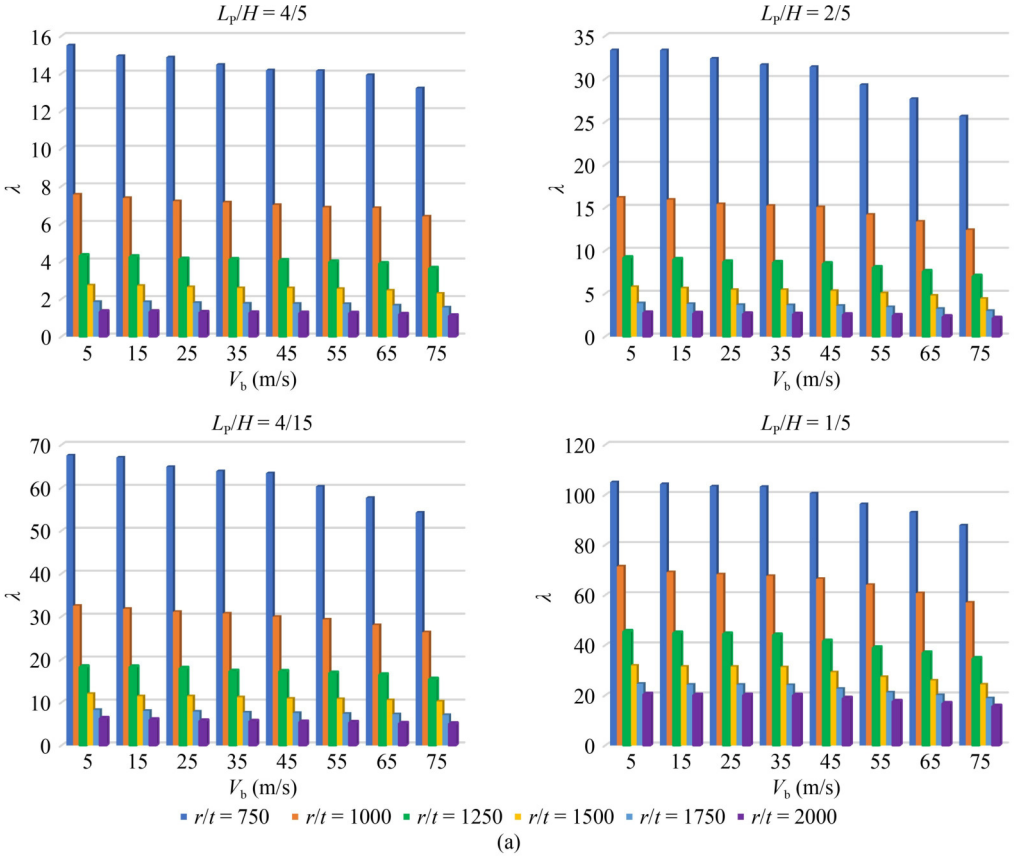
L_p/H = 4/5
L_p/H = 2/5
L_p/H = 4/15
L_p/H = 1/5
λ
V_b (m/s)
r/t = 750
r/t = 1000
r/t = 1250
r/t = 1500
r/t = 1750
r/t = 2000

(a)

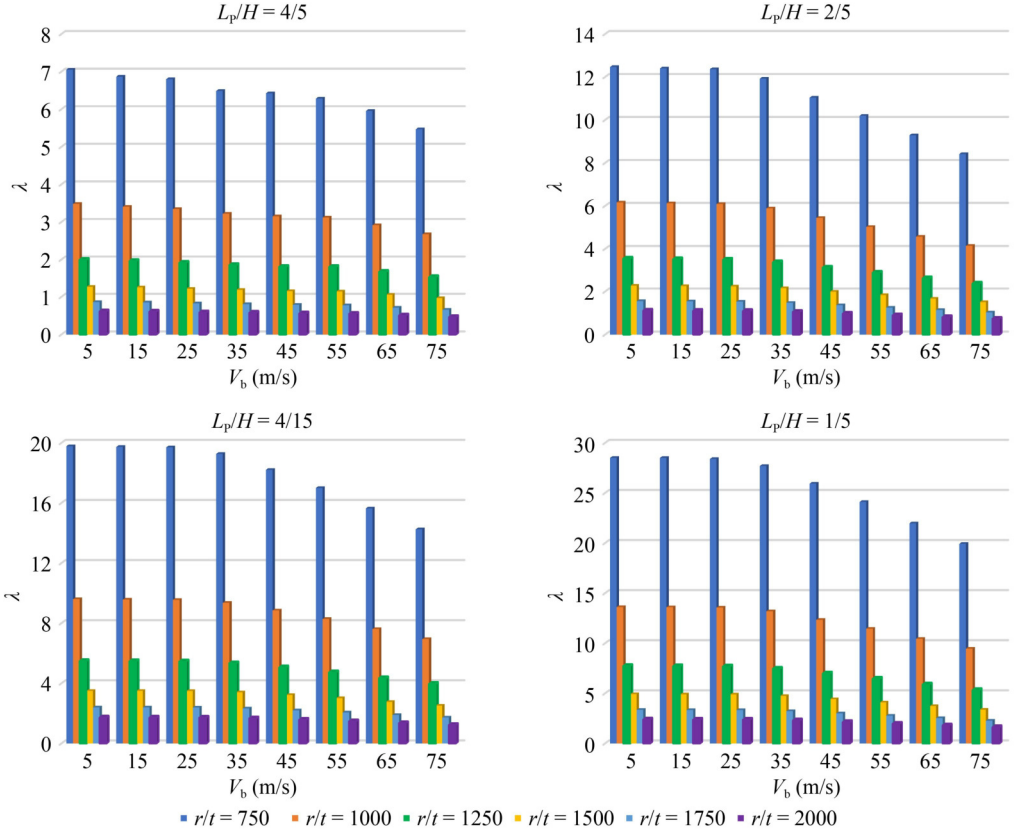
L_p/H = 4/5
L_p/H = 2/5
L_p/H = 4/15
L_p/H = 1/5
λ
V_b (m/s)
r/t = 750
r/t = 1000
r/t = 1250
r/t = 1500
r/t = 1750
r/t = 2000

(b)

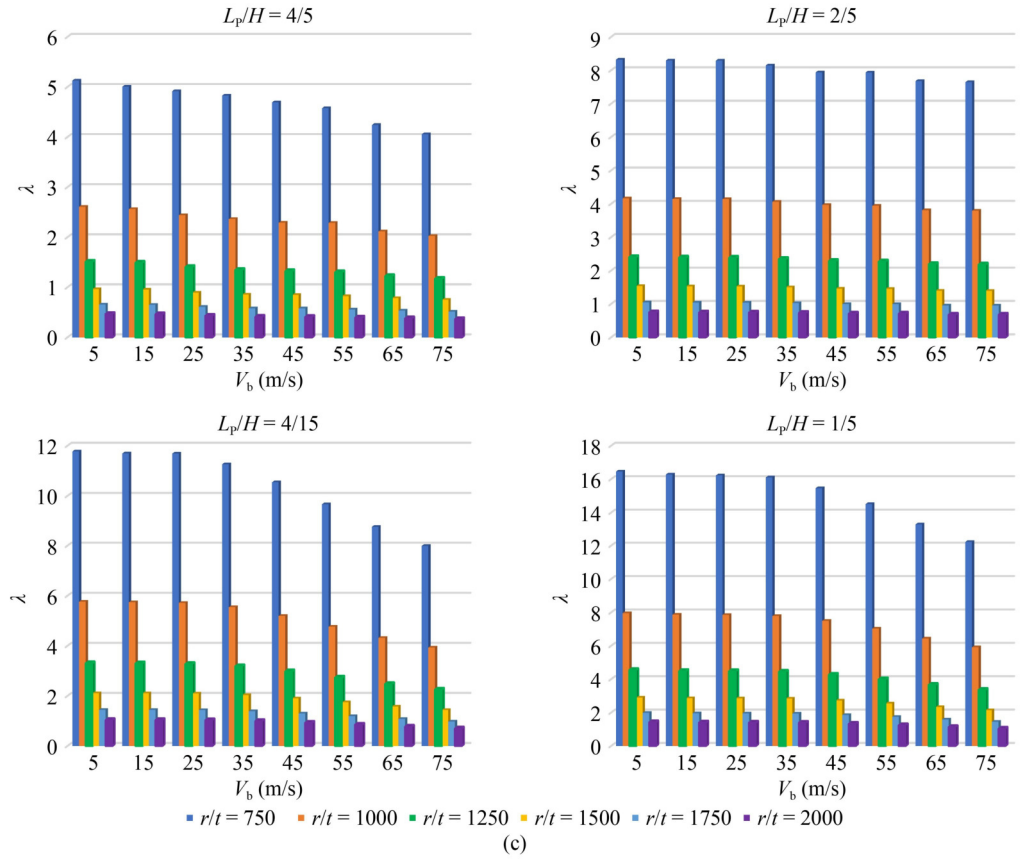

(c)

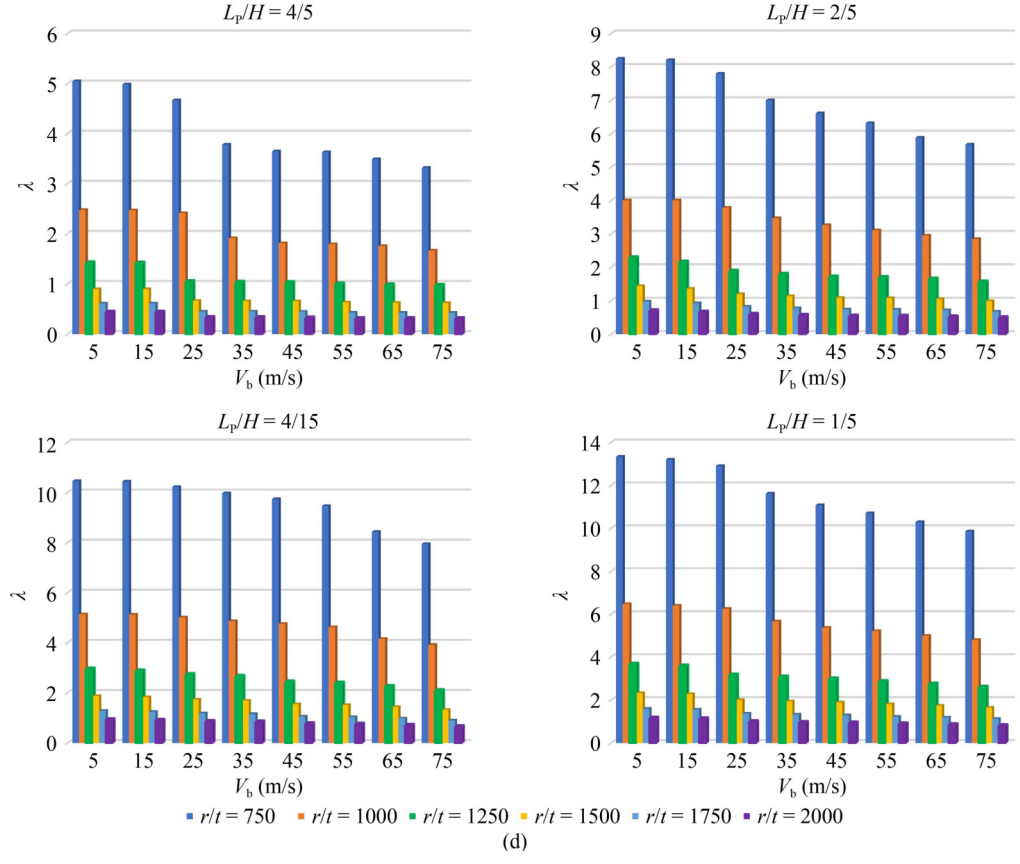

(d)

Fig. 12 Wind induced buckling load multiplier for *H*/*D* ratio: (a) 0.25; (b) 0.5; (c) 0.75; (d) 1.0.

from 4/5 to 1/5, the λ value increases by 79.35%, 59.5%, and 63.4%, accordingly. Gradual increment in r/t ratio from 750 to 2000 reduces the load multiplier value by 50.6%, 42.25%, 36.16%, 31.62%, and 28.41%, accordingly. The λ value decreases by 68.07%, 32.93%, and 17.96%, subsequently for the gradual increase in slenderness ratio from 0.25 to 1.0. As per pressure vessel design guidelines of Moss [80], the safe value of buckling load multiplier should be between 2 to 3. Based on this guideline five distinct stability conditions of tank have been identified in the present study, which are, instability ($\lambda < 1.0$), critical stability ($\lambda =$ or ≈ 1.0), low stability ($1.0 < \lambda \leqslant 2.0$), safe/sufficient stability ($2.0 < \lambda < 3.0$) and high stability ($\lambda \geqslant 3.0$). Instability condition is observed for tank with H/D ratio 0.5, 0.75, and 1.0, for r/t ratio $\geqslant$ 2000, $\geqslant$ 1750, $\geqslant$ 1500, when L_P/H ratio is $\geqslant$ 1/5, respectively.

6.2 Performance of artificial neural network model

The ANN model has been trained with 20%, 40%, 60%, and 80% of 768 data sets obtained from the multiphysics analyses of wind-induced tank-buckling, of which the R and MSE are presented graphically in Figs. 13(a)–13(d), accordingly. Here Y is the predicted output and T is the actual output. The key aspects of training process, such as, tuning of hyperparameter, time duration of training, etc. have been addressed carefully to minimize the risk of model degradation. To lessen the probability of overfitting, single hidden layer of the neural network has

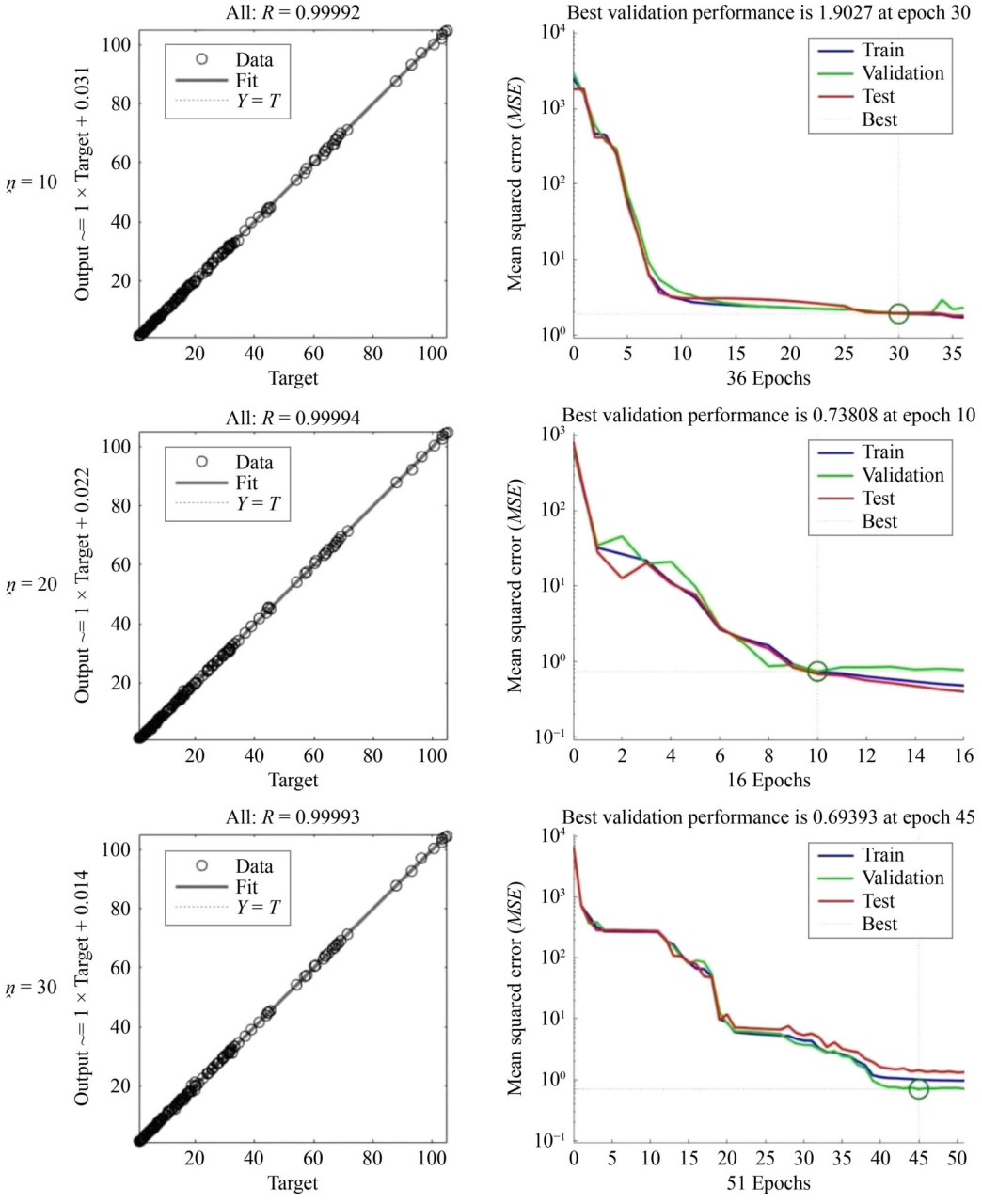

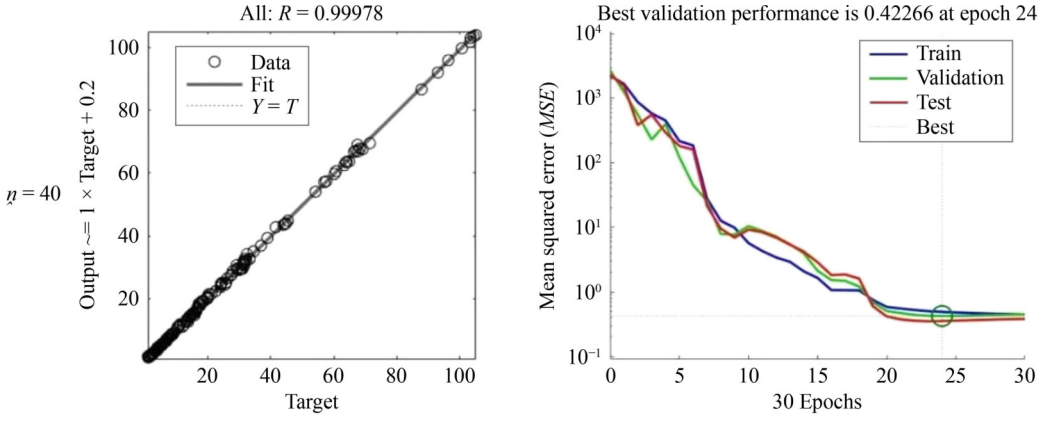

$n = 40$

(a)

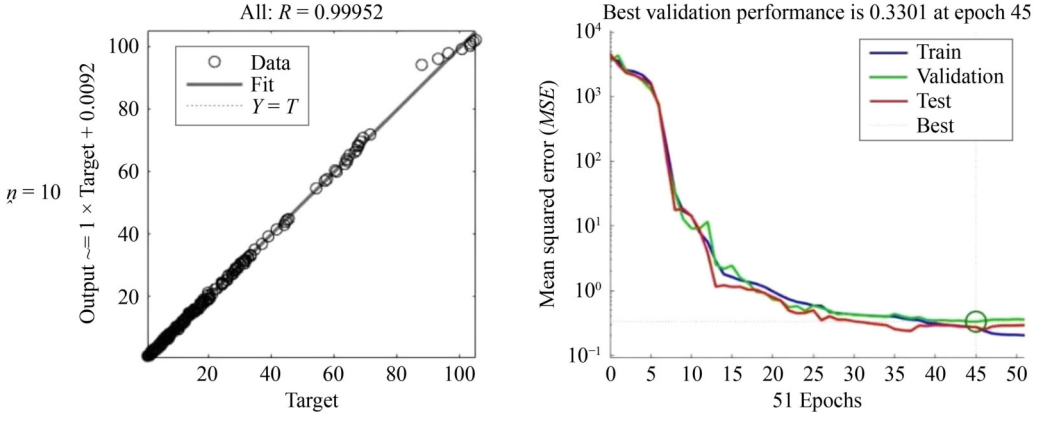

$n = 10$

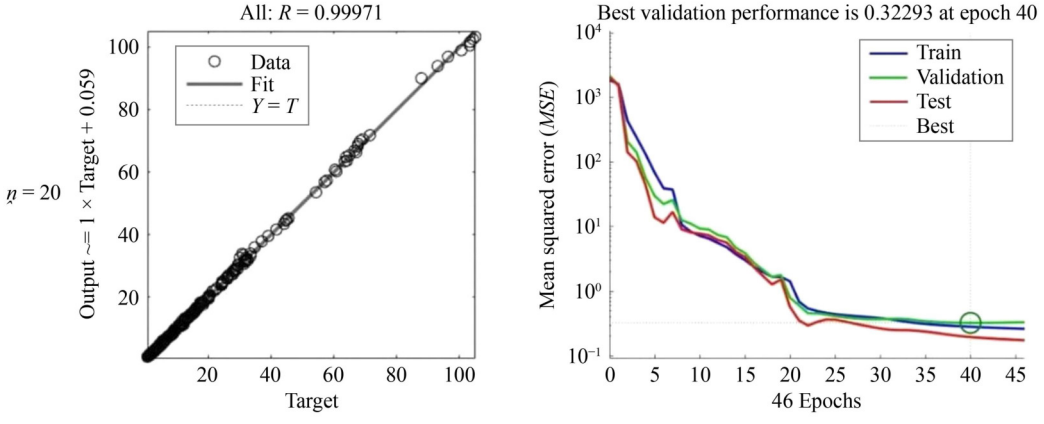

$n = 20$

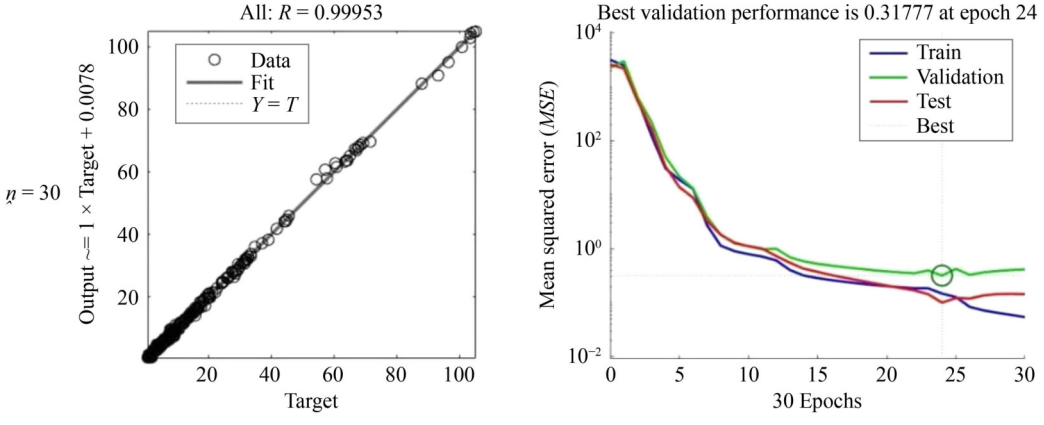

$n = 30$

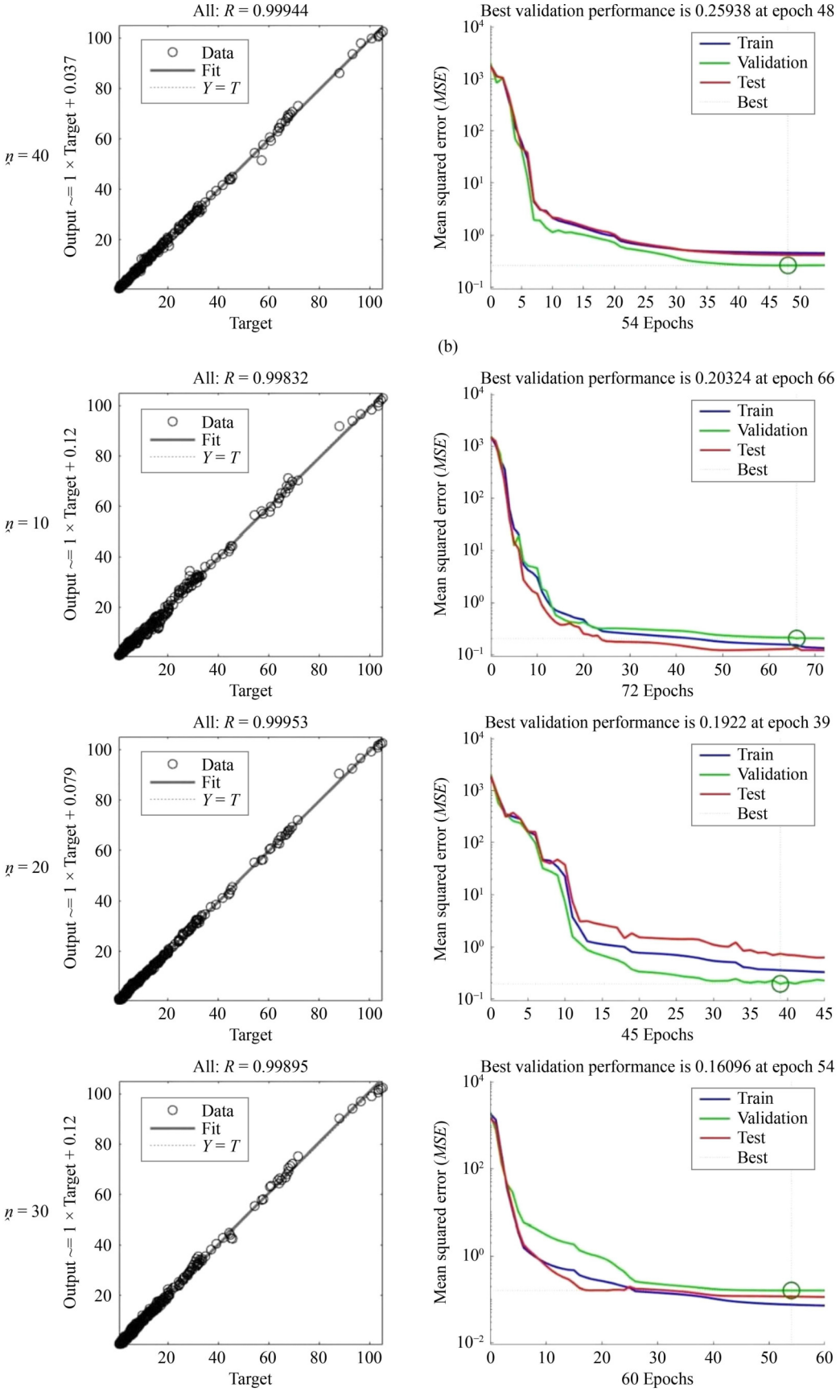
All: R = 0.99944
Output ~= 1 × Target + 0.037
Target
Data
Fit
Y = T
Best validation performance is 0.25938 at epoch 48
Mean squared error (MSE)
54 Epochs
Train
Validation
Test
Best
n = 40
(b)
All: R = 0.99832
Output ~= 1 × Target + 0.12
Target
Best validation performance is 0.20324 at epoch 66
Mean squared error (MSE)
72 Epochs
n = 10
All: R = 0.99953
Output ~= 1 × Target + 0.079
Target
Best validation performance is 0.1922 at epoch 39
Mean squared error (MSE)
45 Epochs
n = 20
All: R = 0.99895
Output ~= 1 × Target + 0.12
Target
Best validation performance is 0.16096 at epoch 54
Mean squared error (MSE)
60 Epochs
n = 30

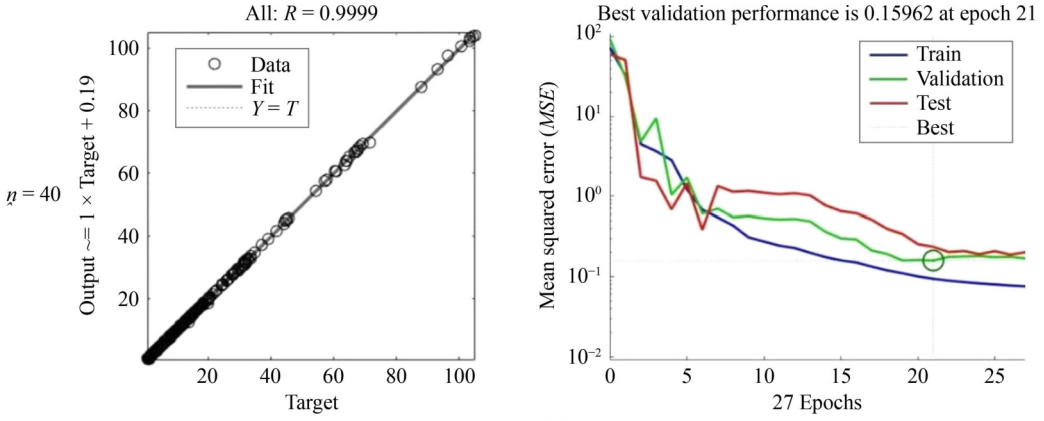
All: R = 0.9999
Data
Fit
Y = T
Output ~= 1 × Target + 0.19
Target
Best validation performance is 0.15962 at epoch 21
Train
Validation
Test
Best
Mean squared error (MSE)
27 Epochs

(c)

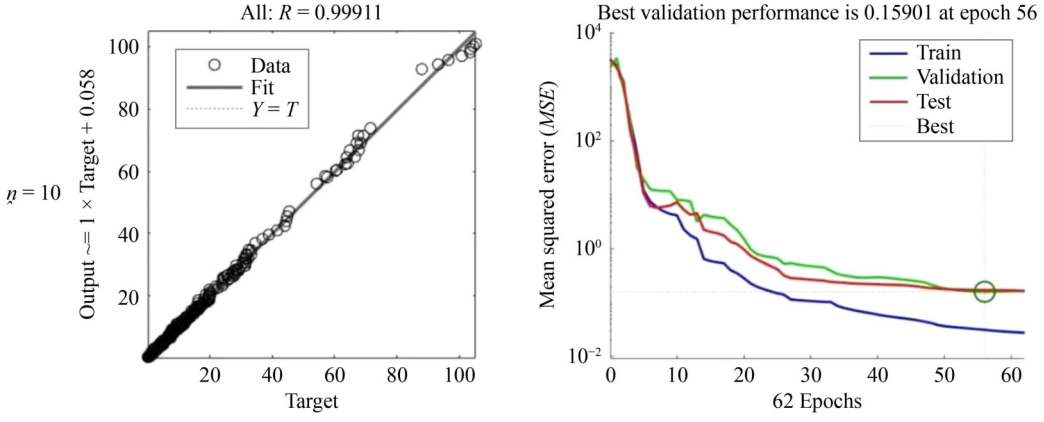
All: R = 0.99911
Data
Fit
Y = T
Output ~= 1 × Target + 0.058
Target
Best validation performance is 0.15901 at epoch 56
Train
Validation
Test
Best
Mean squared error (MSE)
62 Epochs

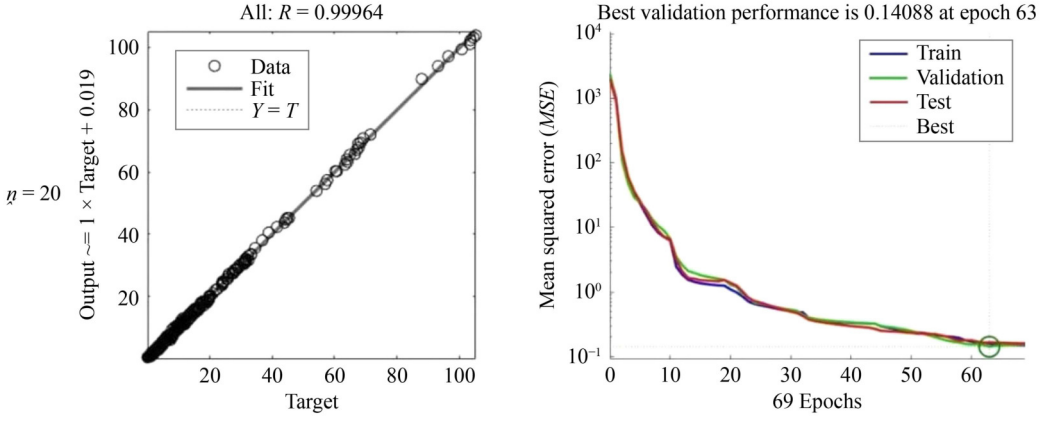
All: R = 0.99964
Data
Fit
Y = T
Output ~= 1 × Target + 0.019
Target
Best validation performance is 0.14088 at epoch 63
Train
Validation
Test
Best
Mean squared error (MSE)
69 Epochs

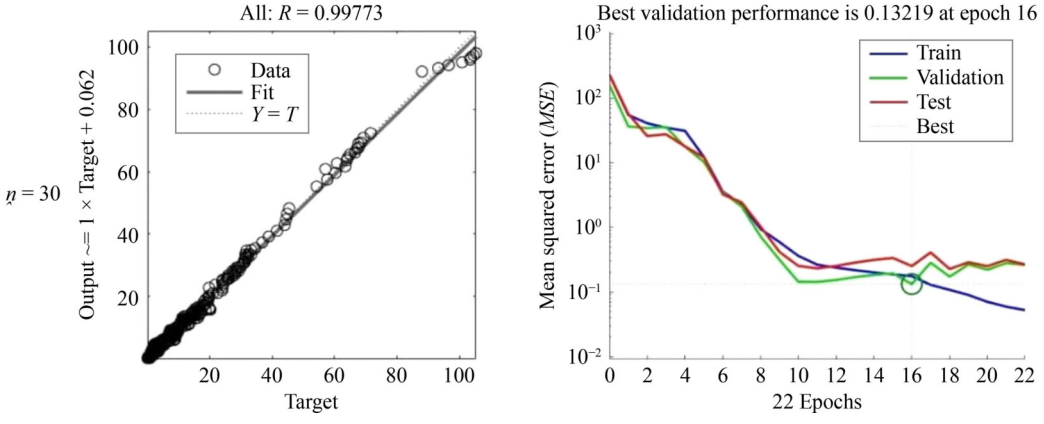
All: R = 0.99773
Data
Fit
Y = T
Output ~= 1 × Target + 0.062
Target
Best validation performance is 0.13219 at epoch 16
Train
Validation
Test
Best
Mean squared error (MSE)
22 Epochs

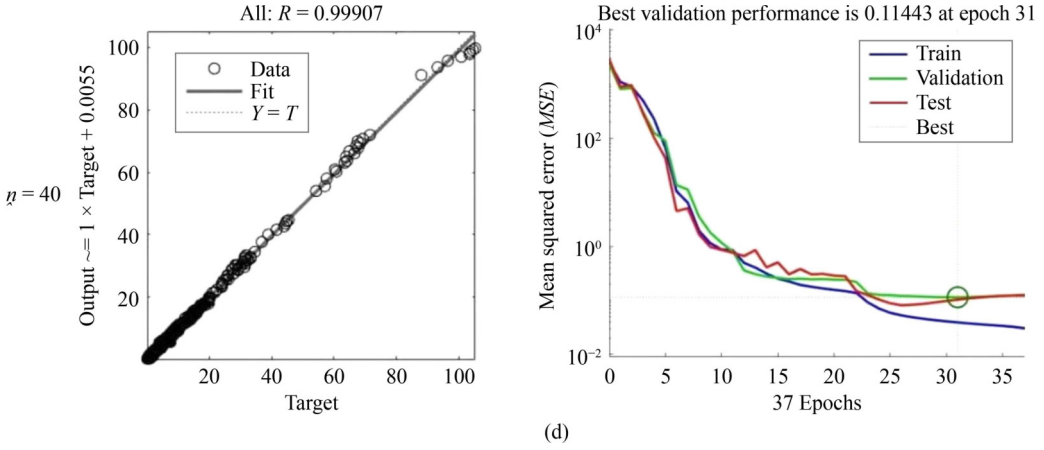

Fig. 13 Performance matrices of ANN for percentage of data set: (a) 20%; (b) 40%; (c) 60%; (d) 80%.

been used. Variation in percentage of data and number of neurons have been applied while training to determine the optimum network, which can address the computational complexity, and challenges in gradient propagation. The best performance based on *MSE* and *R* is observed for 20 neurons with 80% data set at 63rd epoch. Whereas, 30 neurons with 60% data set provides sufficient performance at 54th epoch.

After determining the optimum architecture of the neural network, random tests have been carried out to predict load multipliers of wind-induced buckling of an open-top tank with *H*/*D* ratio 1.25 under basic wind velocity 45 m/s, considering all the combinations of *r*/*t* ratio and L_P. The random test results of buckling load multiplier, produced by proposed ANN model, have been compared with the same obtained through the WSI analyses on similar configuration of tank under V_b 45 m/s, to escalate the proposed ANN model's accuracy, which featured in Fig. 14. 0.61%, 1.57%, 0.3%, and 1.4% error of ANN model has been noticed with respect to WSI analyses for L_P/H ratio 4/5, 2/5, 4/15, and 1/5, respectively. The contours of $\delta_{r_{BN}}$ of the tank with *H*/*D* ratio 1.25 for each test case of L_P/H ratio, are accordingly provided in Figs. 15(a)–15(d), which have been obtained from the WSI analyses. Figures 14 and 15 signifies that in case of *H*/*D* ratio 1.25, open-top, cylindrical, steel tank is

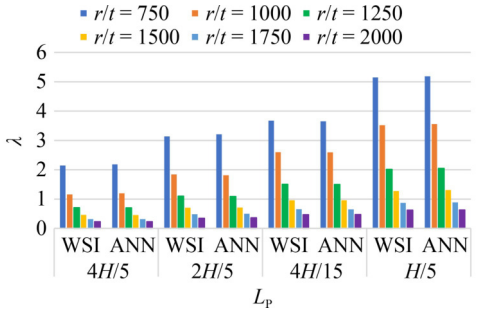

Fig. 14 Comparison of WSI and ANN data of buckling load multiplier for *H*/*D* ratio 1.25.

safe ($2 < \lambda < 3$) against wind-induced buckling under 45 m/s basic speed of wind, when *r*/*t* and L_P/H ratios are 1000 and 4/15, respectively.

7 Conclusions

It is observed that windward region is the most affected portion of a tank against wind-induced buckling. Nondimensional radial deformation is very much useful parameter to escalate the damage of the tank-wall due to wind-induced buckling. Load multiplier is the most reliable parameter for assessing the stability of tank

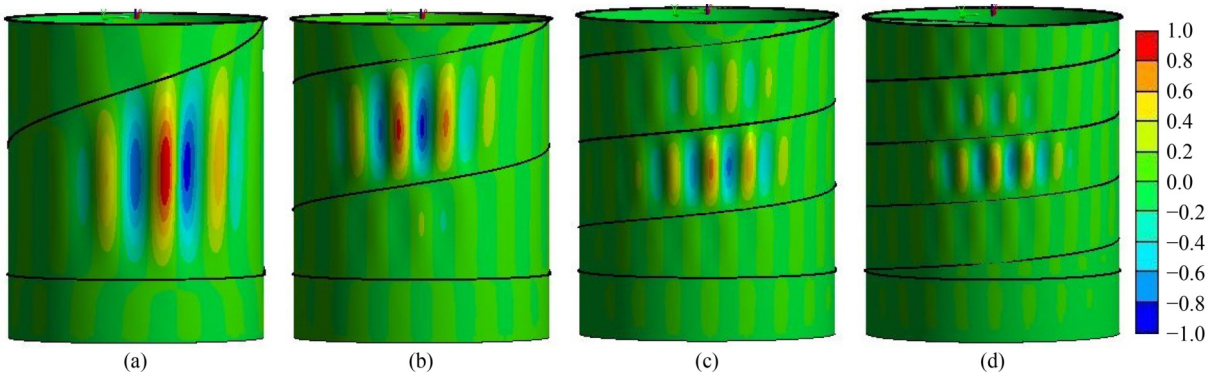

Fig. 15 $\delta_{r_{BN}}$ of open-roof, helically-stiffened tank (*H*/*D* = 1.25) for L_P/H: (a) 4/5; (b) 2/5; (c) 4/15; (d) 1/5.

against wind-induced buckling.

This study highlights that RNA-inspired stiffening-helix can be an effective alternative to ring-stiffener for providing capacity against wind-induced buckling to cylindrical steel tanks. It is reported that wind-induced buckling capacity of open-top, cylindrical, ground-supported, steel tank increases with the decrease in basic wind speed (V_b), H/D, r/t, and L_P/H ratio.

This study can be helpful to determine which nondimensional specifications (H/D, r/t, and L_P/H) are necessary for the safe and economic construction of a tank strengthened with stiffening-helix based on the basic wind speed (V_b) region, in which that tank need to be constructed.

Considering most severe wind speed situation, the most economic while safe combination of r/t and L_P/H ratio is 2000 and 4/15, respectively for tank's H/D ratio 0.25. Similarly, under 75 m/s wind speed, safety with economy can be provided to tanks with H/D ratio 0.5, 0.75, and 1.0, for r/t ratio 1750, 1500, and 1250, when the L_P/H ratio is 1/5, respectively.

With 99.11% accuracy, the proposed ANN model can greatly aid the structural engineers to design open-top, cylindrical, ground-supported, steel tank considering wind-induced buckling by providing load multiplier values in very less amount of time compared to the cumbersome and too much time-consuming WSI analyses.

Competing interests The authors declare that they have no competing interests.

References

1. Jerath S, Sadid H. Buckling of orthotropic cylinders due to wind load. Journal of Engineering Mechanics, 1985, 111(5): 610–622
2. Krajcinovic D. Semimembrane analysis of cylindrical shells subjected to wind loading. Journal of Applied Mechanics, 1970, 37(4): 995–1001
3. Pecknold D A. Load transfer mechanisms in wind-loaded cylinders. Journal of Engineering Mechanics, 1989, 115(11): 2353–2367
4. Pircher M. Medium-length thin-walled cylinder under wind loading—A case study. Journal of Structural Engineering, 2004, 130(12): 2062–2069
5. Uematsu Y, Uchiyama K. Deflection and buckling behavior of thin, circular cylindrical shells under wind loads. Journal of Wind Engineering and Industrial Aerodynamics, 1985, 18(3): 245–261
6. Briassoulis D, Pecknold D A. Behaviour of empty steel grain silos under wind loading: Part 1: The stiffened cylindrical shell. Engineering Structures, 1986, 8(4): 260–275
7. Chen L, Rotter J M. Buckling of anchored cylindrical shells of uniform thickness under wind load. Engineering Structures, 2012, 41: 199–208
8. Maleki S, Mehretehran A M. 3D wind buckling analysis of long steel corrugated silos with vertical stiffeners. Engineering Failure Analysis, 2018, 90: 156–167
9. Uchiyama K, Uematsu Y, Orimo T. Experiments on the deflection and buckling behavior of ring-stiffened cylindrical shells under wind pressure. Journal of Wind Engineering and Industrial Aerodynamics, 1987, 26(2): 195–211
10. Schmidt H, Binder B, Lange H. Postbuckling strength design of open thin-walled cylindrical tanks under wind load. Thin-Walled Structures, 1998, 31(1–3): 203–220
11. Maleki S, Mehretehran A M. 3D wind buckling analysis of steel silos with stepped walls. Thin-Walled Structures, 2019, 142: 236–261
12. Burgos C A, Batista-Abreu J C, Calabró H D, Jaca R C, Godoy L A. Buckling estimates for oil storage tanks: Effect of simplified modeling of the roof and wind girder. Thin-Walled Structures, 2015, 91: 29–37
13. Slowinski K, Piekarczyk M, Dybel P. Effect of simplified wind girder modelling on MNA-LBA analysis of open steel tanks. International Journal of Pressure Vessels and Piping, 2023, 203: 104941
14. Resinger F, Greiner R. Buckling of wind loaded cylindrical shells—Application to unstiffened and ring-stiffened tanks. In: Ramm E, ed. Buckling of Shells. Berlin: Springer, 1982, 305–331
15. Schneider W, Zahlten W. Load-bearing behaviour and structural analysis of slender ring-stiffened cylindrical shells under quasi-static wind load. Journal of Constructional Steel Research, 2004, 60(1): 125–146
16. Azzuni E, Guzey S. Stability of open top cylindrical steel storage tanks: Design of top wind girder. Journal of Pressure Vessel Technology, 2017, 139(3): 031207–031217
17. Sun T, Azzuni E, Guzey S. Stability of open-topped storage tanks with top stiffener and one intermediate stiffener subject to wind loading. Journal of Pressure Vessel Technology, 2018, 140(1): 011204–011217
18. Uematsu Y, Yamaguchi T, Yasunaga J. Effects of wind girders on the buckling of open-topped storage tanks under quasi-static wind loading. Thin-Walled Structures, 2018, 124: 1–12
19. Bu F, Qian C. A rational design approach of intermediate wind girders on large storage tanks. Thin-Walled Structures, 2015, 92: 76–81
20. Bu F, Qian C. On the rational design of the top wind girder of large storage tanks. Thin-Walled Structures, 2016, 99: 91–96
21. Zeybek Ö, Topkaya C, Rotter J M. Stress resultants for wind girders in open-top cylindrical steel tanks. Engineering Structures, 2019, 196: 109347
22. Zeybek Ö, Topkaya C. Stiffness requirements for wind girders in open-top cylindrical steel tanks. Thin-Walled Structures, 2022, 176: 109353
23. Yen S. Buckling of cylindrical shells with spiral stiffeners under uniform compression and torsion. Computers & Structures, 1980, 11(6): 587–595
24. Shaterzadeh A, Foroutan K. Post-buckling of cylindrical shells with spiral stiffeners under elastic foundation. Structural Engineering and Mechanics, 2016, 60(4): 615–631
25. Shaterzadeh A, Foroutan K, Ahmadi H. Nonlinear static and dynamic thermal buckling analysis of spiral stiffened functionally

graded cylindrical shells with elastic foundation. International Journal of Applied Mechanics, 2019, 11(1): 1950005
26. Ahmadi H, Foroutan K. Nonlinear vibration of stiffened multilayer FG cylindrical shells with spiral stiffeners rested on damping and elastic foundation in thermal environment. Thin-Walled Structures, 2019, 145: 106388
27. Ahmadi H, Foroutan K. Nonlinear primary resonance of spiral stiffened functionally graded cylindrical shells with damping force using the method of multiple scales. Thin-Walled Structures, 2019, 135: 33–44
28. Nam V H, Phuong N T, van Minh K, Hieu P T. Nonlinear thermo-mechanical buckling and post-buckling of multilayer FGM cylindrical shell reinforced by spiral stiffeners surrounded by elastic foundation subjected to torsional loads. European Journal of Mechanics. A, Solids, 2018, 72: 393–406
29. Tu T M, Thai D K, Hoan P V, Hoa L K. Nonlinear behavior of FG porous cylindrical sandwich shells reinforced by spiral stiffeners under torsional load including thermal effect. Mechanics of Advanced Materials and Structures, 2022, 29(27): 5860–5875
30. Foroutan K, Dai L. Nonlinear torsional stability and buckling of spiral stiffened sigmoid FG thin circular cylindrical shells. European Journal of Mechanics. A, Solids, 2024, 106: 105328
31. API Standard 650. Welded Tanks for Oil Storage. Washington, D.C.: American Petroleum Institute, 2020
32. Khan A K, Shah T R, Khosa A A, Ali H M. Evaluation of wind load effects on solar panel support frame: A numerical study. Engineering Analysis with Boundary Elements, 2023, 153: 88–101
33. Baiz P M, Aliabadi M H. Buckling analysis of shear deformable shallow shells by the boundary element method. Engineering Analysis with Boundary Elements, 2007, 31(4): 361–372
34. Hu G, Kwok K C. Predicting wind pressures around circular cylinders using machine learning techniques. Journal of Wind Engineering and Industrial Aerodynamics, 2020, 198: 104099
35. Mukherjee S, Reddy J S K, Singha Roy D K. Prediction of wind-pressure coefficients on circular elevated-tanks through the novel CFD-ANN model for various building-interference circumstances. International Journal of Computational Fluid Dynamics, 2023, 37(5): 367–394
36. Waszczyszyn Z, Bartczak M. Neural prediction of buckling loads of cylindrical shells with geometrical imperfections. International Journal of Non-Linear Mechanics, 2002, 37(4–5): 763–775
37. Tahir Z R, Mandal P. Artificial neural network prediction of buckling load of thin cylindrical shells under axial compression. Engineering Structures, 2017, 152: 843–855
38. Tahir Z R, Mandal P, Adil M T, Naz F. Application of artificial neural network to predict buckling load of thin cylindrical shells under axial compression. Engineering Structures, 2021, 248: 113221
39. Tao F, Liu X, Du H, Yu W. Physics-informed artificial neural network approach for axial compression buckling analysis of thin-walled cylinder. AIAA Journal, 2020, 58(6): 2737–2747
40. Liu F, Chen H, Yang J, Wang X. Application of physics-informed machine learning methods in buckling design of axially compressed cylindrical shells. Thin-Walled Structures, 2024, 200: 111963
41. Samaniego E, Anitescu C, Goswami S, Nguyen-Thanh V M, Guo H, Hamdia K, Zhuang X, Rabczuk T. An energy approach to the solution of partial differential equations in computational mechanics via machine learning: Concepts, implementation and applications. Computer Methods in Applied Mechanics and Engineering, 2020, 362: 112790
42. Mishra A, Anitescu C, Budarapu P R, Natarajan S, Vundavilli P R, Rabczuk T. An artificial neural network based deep collocation method for the solution of transient linear and nonlinear partial differential equations. Frontiers of Structural and Civil Engineering, 2024, 18(8): 1296–1310
43. AIJ. Recommendations for Loads on Buildings. Tokyo: Architectural Institute of Japan, 2004
44. Sun X, Li W, Huang Q, Zhang J, Sun C. Large eddy simulations of wind loads on an external floating-roof tank. Engineering Applications of Computational Fluid Mechanics, 2020, 14(1): 422–435
45. Blocken B. LES over RANS in building simulation for outdoor and indoor applications: A foregone conclusion? Building Simulation, 2018, 11(5): 821–870
46. Pasley H, Clark C. Computational fluid dynamics study of flow around floating-roof oil storage tanks. Journal of Wind Engineering and Industrial Aerodynamics, 2000, 86(1): 37–54
47. Kuroda S, Uejima H, Ishida K, Yoshida S, Shiratori M, Sekine K, Tsuchida T, Iwata K. Simulation for a floating roof behavior of cylindrical storage tank due to wind load: Part 1—CFD analysis. In: Proceedings of the ASME 2012 Pressure Vessels and Piping Conference (PVP 2012). Toronto: American Society of Mechanical Engineers, 2012, 125–137
48. Hillewaere J, Degroote J, Lombaert G, Vierendeels J, Degrande G. Computational aspects of simulating wind induced ovalling vibrations in silo groups. Journal of Computational and Applied Mathematics, 2013, 246: 161–173
49. Hillewaere J, Degroote J, Lombaert G, Vierendeels J, Degrande G. Wind-structure interaction simulations of ovalling vibrations in silo groups. Journal of Fluids and Structures, 2015, 59: 328–350
50. Liu Q, Zhao Y, Cai S, Dong S. Wind loads and wind-resistant behaviour of large cylindrical tanks in square-arrangement group. Part 2: CFD simulation and finite element analysis. Wind and Structures, 2020, 31(6): 495–508
51. Sun W, Wang Z, Feng J, Gu W. Surface wind pressure distribution of molten-salt power tower by CFD analysis. Arabian Journal for Science and Engineering, 2022, 47(10): 12497–12507
52. Tominaga Y. Flow around a high-rise building using steady and unsteady RANS CFD: Effect of large-scale fluctuations on the velocity statistics. Journal of Wind Engineering and Industrial Aerodynamics, 2015, 142: 93–103
53. Bairagi A K, Dalui S K. Wind environment around the setback building models. Building Simulation, 2021, 14(5): 1525–1541
54. Hassan S, Molla M M, Nag P, Akhter N, Khan A. Unsteady RANS simulation of wind flow around a building shape obstacle. Building Simulation, 2022, 15(2): 291–312
55. Indian Standard Code IS 875-2015. Code of Practice for Design Loads (Other Than Earthquake Loads), for Building and Structures, Part 3—Wind loads. New Delhi: Bureau of Indian Standards, 2020
56. ANSYS, Inc. CFX-Solver: Ansys Theory Guide Release II, 2006

57. Portela G, Godoy L A. Wind pressure and buckling of grouped steel tank. Wind and Structures, 2007, 10(1): 23–44
58. Bairagi A K, Dalui S K. Prediction of pressure coefficient on setback building by artificial neural networks. Canadian Journal of Civil Engineering, 2021, 48(10): 1364–1385
59. Portela G, Godoy L A. Wind pressure and buckling of cylindrical steel tanks with a conical roof. Journal of Constructional Steel Research, 2005, 61(6): 786–807
60. Franke J, Hellsten A, Schlunzen K H, Carissimo B. The cost 732 best practice guideline for CFD simulation of flows in the urban environment: A summary. International Journal of Environment and Pollution, 2011, 44(1–4): 419–427
61. Indian Standard Code IS SP 64-2001. Explanatory Handbook on Indian Standard Code of Practice for Design Loads (Other Than Earthquake Loads) for Buildings and Structures, Part 3—Wind Loads. New Delhi: Bureau of Indian standards, 2001
62. Song Z J, Xu T L, Ren X H, Xu R J, Li X B. Load-end shortening curve of stiffener elements with beam−column buckling considering steel grades based on empirical formulae of critical stress. Ocean Engineering, 2024, 306: 118115
63. Indian Standard Code IS 803-1976. Indian standard Code of Practice for Design, Fabrication and Erection of Vertical Mild Steel Cylindrical Welded Oil Storage Tanks. New Delhi: Bureau of Indian Standards, 1976
64. Chen S, Deng Y, Liang X. Finite element analysis of birdcage buckling of umbilical cable with damaged sheath. Ocean Engineering, 2024, 304: 117777
65. Zeng J, Yang Y, Ma H, Yang Y, Fan C. Dynamic modelling strategy of a shaft-disk-blade coupling system integrating beam and shell theories. International Journal of Mechanics and Materials in Design, 2024, 20(1): 107–127
66. Gerosa F M, Marsden A L. A mechanically consistent unified formulation for fluid-porous-structure-contact interaction. Computer Methods in Applied Mechanics and Engineering, 2024, 425: 116942
67. Moherdaui T F, Neto A G, Wriggers P. A second-order penalty-based node-to-segment contact using the virtual element method. Finite Elements in Analysis and Design, 2024, 237: 104183
68. Lv H, Zhang H, Zhu Z Y, Dong S L, Xie X. Structural morphologyand dynamic characteristics analysis of drum-shaped honeycomb-type III cable dome with quad-strut layout. Advanced Steel Construction: An International Journal, 2024, 20(1): 81–92
69. Mukherjee S, Mondal U, Roy D K S. Proposition of economic ring-stiffener cross-section to meet the requirements of wind-buckling stability of open-top cylindrical tank. Asian Journal of Civil Engineering, 2024, 25(7): 5089–5107
70. Sun B, Ma D, Gao L, He M, Peng Z, Li X, Wang W. Wind buckling analysis of a large-scale open-topped steel tank with harmonic settlement-induced imperfection. Buildings, 2022, 12(11): 1973
71. Mukherjee S, Singha Roy D K. Wind-structure interaction mechanism of circular storage shells—A critical review. Mechanics of Advanced Materials and Structures, 2024, 31(30): 13284–13307
72. Yang L, Luo Y, Qiu T, Zheng H, Zeng P A. Novel analytical study on the buckling of cylindrical shells subjected to arbitrarily distributed external pressure. European Journal of Mechanics. A, Solids, 2022, 91: 104406
73. Yang L. Analytical investigation on the buckling of cylindrical shells under combined non-uniform axial compression and external pressure. Proceedings of the Institution of Mechanical Engineers, Part C: Journal of Mechanical Engineering Science, 2023, 237(24): 6009–6019
74. Yasunaga J, Uematsu Y. Dynamic buckling of cylindrical storage tanks under fluctuating wind loading. Thin-Walled Structures, 2020, 150: 106677
75. Firouzi N, Lenci S, Amabili M, Rabczuk T. Nonlinear free vibrations of Timoshenko–Ehrenfest beams using finite element analysis and direct scheme. Nonlinear Dynamics, 2024, 112(9): 7199–7213
76. Firouzi N, Dohnal F. Dynamic stability of the Mindlin-Reissner plate using a time-modulated axial force. Mechanics Based Design of Structures and Machines, 2025, 53(1): 446–463
77. Chen H, Chen G, Yang D, Fu Z. Neural network-based DPIM for uncertainty quantification of imperfect cylindrical stiffened shells with multiple random parameters. Engineering Analysis with Boundary Elements, 2024, 166: 105795
78. Hasanzadehshooiili H, Lakirouhani A, Šapalas A. Neural network prediction of buckling load of steel arch-shells. Archives of Civil and Mechanical Engineering, 2012, 12(4): 477–484
79. Pal A, Kundu T, Datta A K. Damage localization in rail section using single AE sensor data: An experimental investigation with deep learning approach. Nondestructive Testing and Evaluation, 2024, 39(5): 1088–1106
80. Moss D R. Pressure Vessel Design Manual. Oxford: Gulf Professional Publishing, 2004